GENERAL RELATIVISTIC CORRECTIONS TO FLUX FOR RAPIDLY ROTATING NEUTRON STARS

by

CHARLEE AMASON

A thesis submitted in partial fulfillment of the requirements for the degree of

Master of Science

Department of Physics
University of Alberta

Abstract

Neutron stars (NSs) are the densest known objects which are gravitationally stable (unlike, e.g., black holes, which have undergone gravitational collapse). This makes NSs ideal sites for studying how matter behaves under extreme conditions, in particular a state known as cold dense matter. Since cold dense matter cannot be produced on Earth, its equation of state (EOS) is one of the most highly sought after equations in physics. Measuring the exact radius R of a NS with mass M will impose significant constraints on the EOS. One method of calculating NS radii involves measuring the variations in light emitted from the surface of a NS as it rotates; this allows us to determine a parameter known as its compactness (M/R). The value of this ratio can be used to rule out possible EOS. By simulating the spectral flux from a NS, we examine how this light is altered by relativistic bending from the star's surface, as well as by spin effects and atmospheric composition.

"Try not to agonize over this, but you need a cool quote."

Sharon Morsink

Acknowledgements

Thank you to my supervisor, **Sharon Morsink**, for your support and guidance; to **Gregory Sivakoff** for much needed pep-talks during my first year in this program; to **Craig Heinke** for our discussions of hydrogen atmosphere physics; to my undergraduate professor **Nicole Ackerman** for your encouraging Skype talks; to the **Agnes Scott College Department of Physics**; to the **University of Alberta Department of Physics** and the astrophysics group within that department; to **Kenny Van** and **Cory Zhao** especially for your eternal willingness to help debug my code; to my parents, **Lee and Tia Amason**, who drove a U-haul all the way from Atlanta to get me here; to my friends, especially **Ashton Freed**, who kept me sane; to the NSERC for the funding and travel opportunities which allowed me to present this research at CASCA in June of 2019, and to the **Faculty of Graduate Studies and Research** and the **Graduate Student Association** for providing a system of support. Finally, a special thanks to my cat, **Nerys**, without whose invaluable insight into the nature of the universe this thesis would never have been finished.

Contents

List of Tables

List of Figures

Chapter 1

Introduction

1.1 Neutron Stars

Neutron stars (NSs) are some of the most interesting objects in the universe. First hypothesized by Baade & Zwicky (1934) and observed by Hewish et al. (1968), a NS is an extremely dense remnant left behind after the death of a massive star. A typical NS is slightly more massive than the sun (1.4 $M_{\odot}$) with a radius the size of a small city (about 12 km). As the name suggests, NSs contain a considerable fraction of neutron matter; however, NS structure is much more complicated than a ball of inert neutrons. NSs are composed of a thin atmosphere (Rajagopal & Romani, 1996), an iron lattice crust (Chen et al., 1974), and a form of matter known as "nuclear pasta," which acts as a transitional phase between the inner crust and nuclear matter deeper inside the star (Watanabe et al., 2000) (see section 1.1.2 for more on nuclear matter). The composition of the NS core is unknown; it may contain ultradense nuclear matter, or the atoms may have decayed into their constituent quarks (Anand et al., 1980; Baym & Chin, 1976). The nature of the matter in the core, and NS structure in general, is determined by its equation of state (EOS).

1.1.1 The NS Equation of State

An EOS describes the relationship between pressure, density, and temperature (P, ρ, and T) for a given phase of matter. One of the simplest and most familiar equations of state is the ideal gas law,

$$P = \frac{\rho k T}{\bar{m}}, \tag{1.1}$$

where $\bar{m}$ is average mass of particles in the gas and k is the Boltzmann constant. The ideal gas law is often used in simplified models of stars. Because NSs are so dense, however, neutron degeneracy supplies a pressure much larger than the pressure from thermal motion (such as the ideal gas law) and the pressure is independent of temperature. A NS EOS can be approximated by a piecewise polytrope

$$P(\rho) = K\rho^{\gamma}, \tag{1.2}$$

where K is a constant and γ is the adiabatic index. This is a piecewise function because there are three different adiabatic indices and subsequently three different density intervals (Read et al., 2009).

The NS EOS is one of the most highly sought equations in astrophysics. Measuring the mass and radius of a NS exactly would allow us to strongly constrain this equation, but the relatively small sizes of NSs and the great distances involved in astrophysics make direct measurement of these properties exceedingly difficult. Sometimes mass can be measured directly through observation of a NS in a binary, but without sufficient resolving power it is more difficult to measure the radius. Due to this comparative difficulty, methods used for measuring radii are more prone to systematic uncertainties than those used for measuring mass. These various methods of indirect measurement are vital in the effort to constrain the NS EOS (Degenaar & Suleimanov, 2018).

1.1.2 Neutron Degeneracy

If a gas becomes sufficiently dense, the electrons in that gas will be forced to occupy the lowest available energy levels. Because of the Pauli exclusion principle, electrons cannot occupy the same quantum state; as electrons fill up higher energy states, the pressure of the gas will increasingly depend on the nonthermal motions of the electrons instead of temperature (Carroll & Ostlie, 2007). This is known as an electron degenerate gas, or Fermi gas. A star comprised of degenerate matter has many interesting properties—for example, a star with more mass will have a smaller radius compared to a star with less mass. White dwarf (WD) stars are supported by electron degeneracy pressure. Neutron stars are supported by a different kind of degeneracy pressure known as neutron degeneracy pressure.

Inside a NS, densities are even higher than in WDs; a typical NS will have an average density on par with that of an atomic nucleus ($\sim 10^{14}$ g/cm^3) (Carroll & Ostlie, 2007). In these conditions, it is favorable for protons and electrons to form neutrons through a process known as inverse beta decay. Though some of these new neutrons will attach to existing nuclei to form neutron-heavy isotopes (a process known as neutronization), others will exist in the NS as a fluid of free neutrons in the inner crust (Carroll & Ostlie, 2007). Like electrons, neutrons must also occupy particular quantum states. NSs are supported against gravity by this neutron degeneracy pressure.

1.1.3 Superfluidity and Superconduction

Free neutrons in a degenerate neutron fluid may spontaneously pair, such that they act as one boson instead of two fermions. These paired neutrons will not be subject to the Pauli exclusion principle, and can thus fill the lowest energy state without limit. This means that the fluid flows without friction, so it cannot lose energy via friction. A fluid with this property is known as a superfluid.

Motion inside of a superfluid NS interior will continue indefinitely, as there is no viscosity to slow it down (Carroll & Ostlie, 2007).

Deeper inside the neutron star, where the density approaches nuclear densities, the barrier between individual nuclei and the superfluid becomes indistinguishable. When protons pair to form bosons, the resulting fluid is superconducting—i.e., it has no electrical resistance (Carroll & Ostlie, 2007). The superfluid portion of the NS interior is thus a perfect conductor of electricity, which has important implications for the strength of its magnetic field.

1.2 Pulsars

As massive stars collapse to form compact objects, the concentration of magnetic field lines increases tremendously. Subsequently, many NSs have very strong magnetic fields—some as high as 10^{14} G (Harding & Lai, 2006). Due to the conservation of angular momentum, NSs also rotate rapidly, with some NSs having spin periods on the order of milliseconds (Alpar et al., 1982). Charged particles (free electrons and positrons) accelerated along the NS magnetic field lines produce radiation which is visible at radio wavelengths. Since this radiation is only seen when it is directed at us (like the beam from a lighthouse), and the magnetic field axis is not aligned with the spin axis, this light appears as regular "pulses" instead of a constant beam. We call these sources pulsars. Though first observed at radio wavelengths, radiation from pulsars spans the whole electromagnetic spectrum; young pulsars like the Crab emit most of their energy in the X-ray (Andrew Lyne & Graham-Smith, 1998). This X-ray emission can be beamed, like the radio emission, or thermal (e.g., from a heated spot on the NS surface). These "hot spots" form when charged particles (electrons and positrons) in the magnetosphere accelerate along the magnetic field lines and collide with the NS surface at the poles. Hot spots can emit very bright X-rays which are thermal in origin, especially when the NS is accreting

material from a companion. Whether or not it has a companion, a NS with pulsed X-ray accretion is sometimes called an X-ray pulsar (Nagase, 1989).

Pulsar emission provides an incredibly accurate method of measuring the NS spin frequency. Repeated measurements can reveal frequency changes, which in turn yields information about the magnetic field, since magnetic dipole radiation is the dominant cause of decreasing spin frequency ("spin down") for rotation-powered pulsars (Ostriker & Gunn, 1969; Gold, 1968). Increases in pulsar frequency have also been observed ("spin up"). For binary systems where the NS is accreting, this may be caused by torque from the accretion disk (Alpar et al., 1982). Isolated systems generally spin down, but "glitches," where the frequency sharply changes before resuming its gradual decrease (or increase), have been observed. These glitches are likely a result of the fact that the solid NS crust and fluid interior do not always rotate at the same rate. If the interior is spinning faster than the crust, and the two regions suddenly become coupled, the frequency will appear to change while the crust catches up with the interior (or vice versa) (Andrew Lyne & Graham-Smith, 1998). This phenomenon is often attributed to superfluidity in the NS (see section 1.1.3).

1.2.1 Other Sources of NS Emission

Neutron stars are associated with many other observable phenomena. X-rays are produced when an accreting NS undergoes an explosion of nucleosynthesis, known as a Type I X-ray burst (Bildsten, 1998). Young neutron stars with very strong magnetic fields may produce soft gamma ray bursts (Duncan & Thompson, 1992). Recently, a NS-NS collision has been observed via gravitational radiation (Abbott et al., 2018); gravitational waves from single NSs are considerably weaker and have not yet been observed. In this work, we are primarily interested in emission from the NS surface, which can be used to deduce the NS radius using the method described in Rutledge et al. (2002). When X-ray binaries are not accreting material, most of the observed emission is from

the NS surface itself. Quiescent low mass X-ray binaries (henceforth qLMXBs) are thus ideal for our purposes. Observations of qLMXBs and the constraints placed on potential NS masses and radii as a result of those observations are described in section 1.3.

1.3 Relevant Observations

qLMXBs have been observed both inside our galaxy and in galactic globular clusters (GCs). Because our calculations require accurate distances, and because there are $\sim$ 100 times more LMXBs per unit mass in GCs (Clark, 1975), we focus on the latter population. The Chandra and XMM-Newton X-ray observatories have allowed for detailed observations of hundreds of X-ray sources in GCs. Compared to other X-ray sources (such as millisecond pulsars), qLMXB have similar colors—where color here describes the difference between the number of flux counts in two specific frequency ranges, akin to, e.g., the B-V color index in optical astronomy. This color measurement serves as a very rough estimate of temperature. Despite this similarity, qLMXBs are much more luminous than millisecond pulsars (MSPs); this makes sense, because qLMXBs emit from the entire NS surface, whilst MSPs only emit from small hot spots. qLMXB luminosities are on order 10^{32-34} erg/s, and the spectra have a thermal component which implies a radius of the expected magnitude ($\sim$ 10 km). Sometimes a harder, nonthermal component can be seen as well, particularly for qLMXBs in the galactic field (Heinke et al., 2003). The exact origin of the X-ray emission is unknown—it might be heat from deep within the NS crust (Brown & Bildsten, 1998), or residual accretion of material from prior outbursts. The nature of the nonthermal component is also unknown, but, as the nonthermal component is less prominent in GC qLMXBs, this is not a major concern. (Note that the relative lack of a nonthermal component is likely a selection effect—due to their abundance, GC qLMXBs are the only

qLMXBs which have been identified during quiescence.)

A sphere with radius R at a distance d that emits as a blackbody with temperature T will have bolometric flux

$$F = \left(\frac{R}{d}\right)^2 \sigma T^4, \tag{1.3}$$

where σ is the Stefan-Boltzmann constant. Measurement of the spectrum gives T, so if flux and distance are known, the radius of the star can be determined. When the thermal component is fit using a blackbody, the inferred radii are much smaller than anticipated (on order of 3 km) (Rutledge et al., 1999). This is likely due to the presence of a hydrogen atmosphere, which forms after the gravitational settling of accreted material. Hydrogen atmosphere models applied to a NS inside a qLMXB yield radii in line with theoretical expectations (Heinke et al., 2006; Zavlin et al., 1996; Rajagopal & Romani, 1996). The magnetic field strength of NSs in qLMXBs is low enough ($B \lesssim 10^8$ G) that the temperature distribution and opacity on the star's surface remain unaffected (Heinke et al., 2006). This allows us to omit magnetic fields from models of qLMXBs and still obtain values in line with observed fluxes. The effect of hydrogen atmospheres on observed spectral and bolometric flux is discussed in detail in section 1.6.

1.4 General Relativistic Effects

Due to their incredible densities, NSs have very high surface gravities (on order $\log_{10} g \sim 14.4$ cm/s^2). The escape velocity from the surface of a NS can thus be a large fraction of the speed of light. This makes Newtonian gravity a poor approximation, since we need to consider the bending of spacetime in order to properly trace the paths of the photons which reach our detector. A general relativistic (GR) model is thus required. The Schwarzschild solution to Einstein's field equations provides the simplest possible GR model; although the

Schwarzschild solution assumes a stationary, spherical object, spin effects can be added in after the metric has been calculated (see section 1.5). This widely used model is known as the Schwarzschild + Doppler (S + D) approximation. Cadeau et al. (2005, 2007) and others have used the S + D model to calculate NS fluxes. The Kerr solution, which allows for a spinning object, does not significantly improve upon the S + D approximation (Cadeau et al., 2007). Since the correct rotating neutron star solution is computationally intensive, using S + D is preferred.

When a photon leaves the surface of a NS, its path is bent by the star's gravity. This results in an increase in observed flux, since some light from the back of the star, which would be invisible under Newtonian gravity, becomes visible in GR. Fu & Taam (1990) found that, aside from gravitational redshift (which is by far the largest effect), light bending is the most important effect when computing GR light curves. The mathematical details of these effects, and the S + D model generally, are discussed in section 2.3.

1.5 Spin Effects

When considering a spinning NS, both Doppler effects and the deformation of the NS shape must be taken into account. Baubock et al. (2015) found that assuming a stationary, spherical NS can result in an underestimate of the radius by as much as 4%. This is because, under the assumption of a fixed equatorial radius, a spinning NS will have a smaller observed flux than a stationary NS. This is primarily because of oblateness (a rapidly rotating star will "flatten out" along the spin axis, resulting in a smaller surface area for an observers at high inclinations). Therefore, the (purely theoretical) spherical, stationary NS required to produce a certain amount of flux will have a smaller equatorial radius compared to an oblate, spinning NS required to produce the same flux. Accurate radii are of vital importance to finding the correct NS EOS, so it is

necessary to include spin effects in our flux model. Baubock et al. (2015) make use of a modified Schwarzschild metric developed by Morsink et al. (2007), appropriately called the Oblate Schwarzschild (OS) approximation, in their flux calculations. Doppler boosting and oblateness are discussed in more detail in sections 2.4.1 and 2.4.2, respectively.

1.6 Hydrogen Atmospheres

Neutron stars have thin atmospheres (on the order of ~ 10 cm), the composition of which is a source of interest for many astrophysicists. If a donor star has no hydrogen (e.g., a helium white dwarf), then the NS may develop a helium atmosphere (Catuneanu et al., 2013). Some NSs may also have carbon atmospheres (Ho & Heinke, 2009). Since heavier nuclei tend to settle to the bottom of the atmosphere, however, most NS atmospheres are predominantly hydrogen; a pure H atmosphere is therefore a good approximation.

A H atmosphere model will have a harder spectrum than a blackbody model with the same effective temperature. This is because free-free absorption has a strong dependence on frequency—i.e., because the H atmosphere absorbs photons at lower frequencies (Rajagopal & Romani, 1996; Zavlin et al., 1996). Although for individual directions of photon emission (e.g., perpendicular to the surface), atmospheric scattering may result in a different value of flux, the H atmosphere and blackbody produce roughly the same bolometric flux when summed over all possible directions of photon emission. The H atmosphere model used in Zavlin et al. (2002) changes radii estimates of NS polar caps by a factor greater than 3 when compared to a blackbody model. The radius inferred by the H atmosphere agrees with theoretical expectations, while the blackbody radius is unrealistically small.

Gonzalez-Caniulef et al. (2019) have found that, for colder NSs ($T \sim 10^5$ K), plasma effects become important in the UV range. These effects have the

result of increasing opacity and subsequently blocking photons below a certain frequency. Because we are primarily concerned with energies $\gtrsim 50$ eV, we do not take these effects into account.

In this thesis, we use a fully ionized H atmosphere as described in Ho & Lai (2001). For the temperature we are considering ($T = 10^6$ K), full ionization is a reasonable assumption.

1.7 Thesis Organization

Chapter 2 delves into the mathematics on which this thesis is based, primarily the calculation of spectral and bolometric flux. This calculation includes Doppler spin effects, gravitational light bending, and gravitational redshift. The spacetime metric used in determining photon paths and the oblateness model for rapidly rotating NSs are also considered. Chapter 3 describes the main work of this thesis, a python program which calculates the flux using the mathematics described in Chapter 2. Chapter 4 describes the results of our simulations. Chapter 5 discusses our conclusions and intentions for future work.

Chapter 2

Mathematical Theory

This chapter details the mathematical background upon which the work of this thesis is based. Section 2.1 describes the geometry used in our calculations; section 2.2 describes how flux from a static star is calculated in Newtonian gravity; section 2.3 describes how flux from a static star is calculated in general relativity; section 2.4 describes the most important spin effects for rotating stars (Doppler boosting and oblateness, in 2.4.1 and 2.4.2, respectively).

2.1 Spin-Aligned Geometry

In this work we use spin-aligned geometry, such that the spin axis is aligned with the z axis in Cartesian space. The spherical coordinate transformations are given by

$$\begin{aligned} x &= r\sin\theta\cos\phi \\ y &= r\sin\theta\sin\phi \\ z &= r\cos\theta, \end{aligned} \tag{2.1}$$

where θ is the polar angle, ϕ is the azimuthal angle, and r is the radial coordinate (See Figure 2.1). Due to light bending, the direction $\hat{k}_0$ at which the photon leaves the surface of the NS is not necessarily the same as the direction at which it reaches our detector $\hat{k}$ (Figure 2.2).

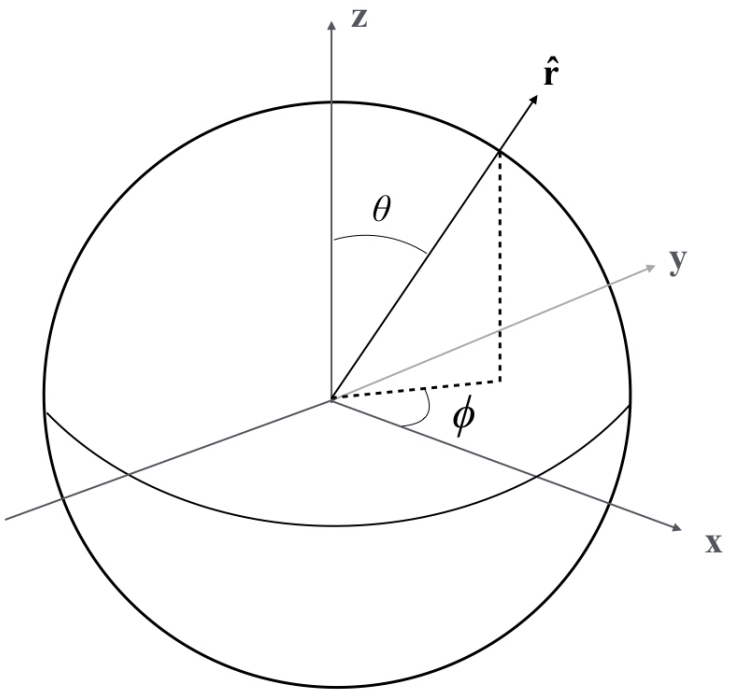

Figure 2.1: A neutron star in spherical coordinates. This is a spin-aligned coordinate system, where the polar angle (θ) is measured from the spin axis (z), such that $\theta = 0$ aligns with the spin axis and $\theta = \pi/2$ aligns with the equator.

The vector $\hat{k}$, which describes the direction of the observer, can be expressed

$$\hat{k} = \sin i \; \hat{x} + \cos i \; \hat{z}, \tag{2.2}$$

which, using the spherical coordinate transformations and the definition of the radial vector $\hat{r} = (x, y, z)$ (note that the radial vector $\hat{r}$ coincides with the normal vector $\hat{n}$ for a spherical surface), yields

$$\begin{aligned} \hat{k} \cdot \hat{r} &= \cos\theta \cos i + \sin\theta \cos\phi \sin i \\ &= \cos\Psi. \end{aligned} \tag{2.3}$$

This relationship is apparent in Figure 2.3, which also includes the inclination angle i, and the zenith angle $\hat{r} \cdot \hat{k}_0 = \cos\alpha$. The impact parameter is given by

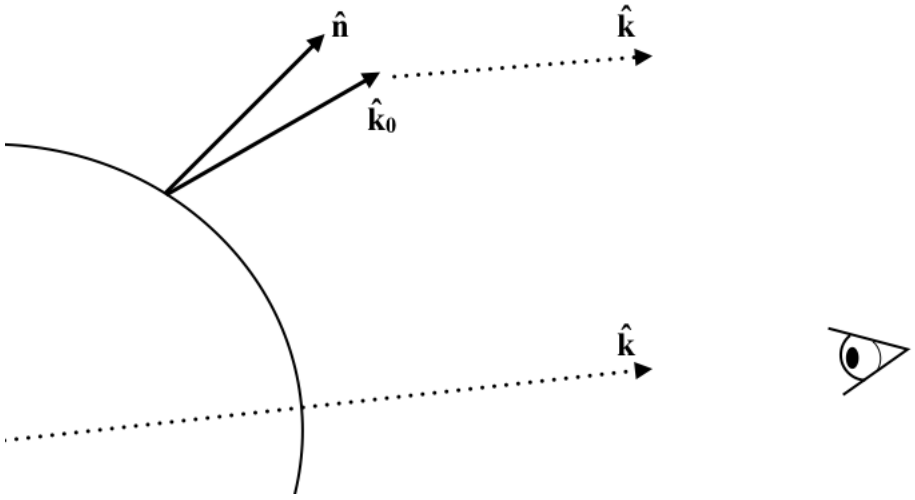

Figure 2.2: A photon leaving the surface of a gravitationally lensed NS in the $\hat{k}_0$ direction will appear to be emitted at a different angle k to an observer at infinity.

(Pechenick et al., 1983a)

$$b = \frac{R \sin \alpha}{\sqrt{1 - 2M/R}}, \tag{2.4}$$

where R is the NS equatorial radius (which is the same as the radius everywhere on the star for a spherical star) and $G = c = 1$. In this case the impact parameter describes the orthogonal distance between the path of our photon and the centre of the gravitational potential (i.e., the centre of our neutron star). The relationship between α and Ψ is described by (Pechenick et al., 1983a)

$$\Psi = \int_R^\infty \frac{dr}{r^2} \Big[\frac{1}{b^2} - \frac{1}{r^2} \Big(1 - \frac{M}{r} \Big) \Big]^{-1/2}, \tag{2.5}$$

where the impact parameter b is a function of α as described above. The Newtonian limit corresponds to the limit $M \to 0$ in the equation above, i.e.,

$$\Psi = \alpha.$$

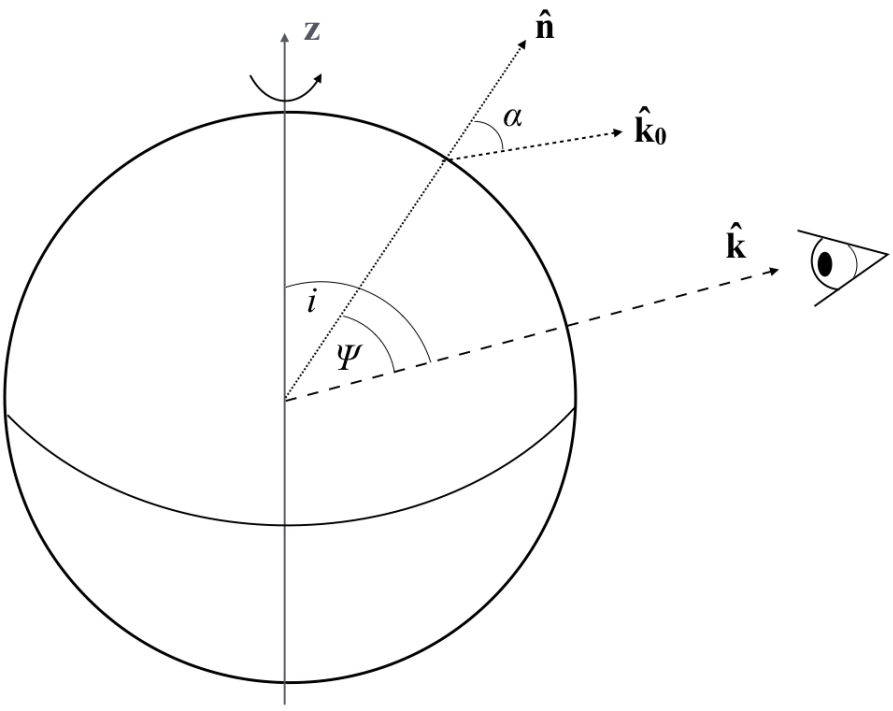

Figure 2.3: Geometry of a neutron star with an observer at infinity in direction $\hat{k}$ and a photon emitted in direction $\hat{k}_0$.

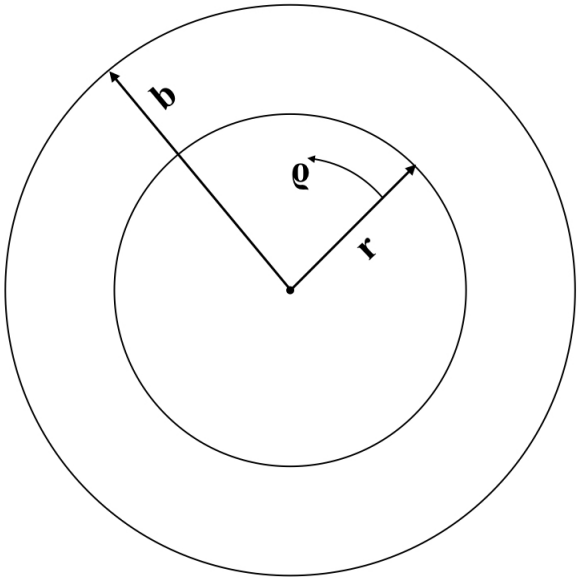

Figure 2.4: A different view of our NS. The vector $\hat{k}$ points out of the page at the centre of the figure, ϱ describes the rotation around the vector $\hat{k}$, and b is the impact parameter. Photons emitted from the star on the circle defined by r appear to the observer to originate from the circle defined by b.

2.2 Flux From a Static NS in Newtonian Gravity

In a Newtonian system, there is no gravitational bending of light from the NS surface ($\hat{k} = \hat{k}_0$). It follows that the impact parameter b is simply

$$b = R \sin \alpha, \tag{2.6}$$

where R is again the NS radius and α is the zenith angle. In Newtonian gravity, it is equivalent to say

$$b = R \sin \Psi, \tag{2.7}$$

since the zenith angle is the same as the bending angle. An infinitesimal section of surface area, dS, is given by

$$dS = R^2 \sin \theta d\theta d\phi. \tag{2.8}$$

The observed solid angle, $d\Omega$, is therefore

$$d\Omega = \frac{dS \cos \alpha}{d^2}, \tag{2.9}$$

where d is the distance between the NS and our detector on Earth. The value of the projection term $\cos \alpha$ will determine whether a photon will be visible from our detector, or if, e.g., it will be emitted from the back of the NS and will therefore be invisible. As stated previously, $\alpha = \Psi$ in Newtonian physics; this means that the available surface for photon emission is equivalent to the NS cross-sectional area πR^2. We will see later this is not the case for a relativistic

star. Taking $\cos\alpha = \cos\Psi$, the differential solid angle becomes

$$\begin{aligned} d\Omega &= \frac{dS\cos\Psi}{d^2} \\ &= \frac{R^2}{d^2}\sin\theta\cos\Psi d\theta d\phi \\ &= \frac{R^2}{d^2}\big(\sin\theta\cos\theta\cos i + \sin^2\theta\cos\phi\sin i\big)d\theta d\phi. \end{aligned} \tag{2.10}$$

For uniform emission from a spherically symmetric star we can choose $i = 0$ without loss of generality. In this case, the differential solid angle is simply

$$d\Omega = \frac{R^2}{d^2}\sin\theta\cos\theta\ d\theta d\phi. \tag{2.11}$$

We assume a blackbody for simplicity. Using a form of Planck's law, we can calculate the specific intensity

$$I_{E,em} = \frac{2}{c^2h^2}E_{em}^3\big(e^{E_{em}/kT} - 1\big)^{-1}, \tag{2.12}$$

where c is the speed of light, h is Planck's constant, k is the Boltzmann constant, E_{em} is the energy of the photon emitted from the surface of the NS, and T is the temperature of the NS, which is assumed to be homogeneous. The value of the integral of $I_{E,em}$ over the energy range 0 to ∞ is known to be (Carroll & Ostlie, 2007)

$$\int_0^\infty I_{E,em}dE_{E,em} = \frac{2}{c^2h^2}\frac{k^4T^4}{h}\frac{\pi^4}{15}. \tag{2.13}$$

The flux dF from a small surface element dS is (Carroll & Ostlie, 2007)

$$dF = I_{E,obs}d\Omega, \tag{2.14}$$

where $I_{E,obs}$ is the observed specific intensity of the radiation. Note that the observed and emitted frequencies are the same in the Newtonian case, i.e.,

(Rybicki & Lightman, 1979)

$$I_{E,em} = I_{E,obs}. \tag{2.15}$$

With subscripts omitted for simplicity, the spectral flux can be expressed

$$F_E = \frac{R^2}{d^2} I_E \iint \sin\theta \cos\theta \; d\theta d\phi. \tag{2.16}$$

The limits of integration are determined by the geometry of the system; but, since all inclinations are identical for a spherical star, it is sufficient to examine $i = 0°$. The spectral flux is thus

$$\begin{aligned} F_E &= \frac{R^2}{d^2} I_E \int_0^{2\pi} \int_0^{\pi/2} \sin\theta \cos\theta \; d\theta d\phi \\ &= \frac{R^2}{d^2} \pi I_E. \end{aligned} \tag{2.17}$$

For the same geometry, bolometric flux over the energy range 0 to ∞ is

$$F_{bolo} = \frac{R^2}{d^2} \pi \int_0^{\infty} I_E \; dE. \tag{2.18}$$

Using the known value of the specific intensity integral (equation 2.13), this becomes

$$\begin{aligned} F_{bolo} &= \frac{R^2}{d^2} \frac{2}{c^2 h^2} \frac{k^4 T^4}{h} \frac{\pi^4}{15} \pi \\ &= \frac{R^2}{d^2} \frac{2\pi^5 k^4}{15 c^2 h^3} T^4, \end{aligned} \tag{2.19}$$

which, allowing $\sigma = 2\pi^5 k^4 / 15 c^2 h^3$ and the addition of the distance term R^2/d^2, gives the familiar Stefan-Boltzmann law

$$F_{bolo} = \frac{R^2}{d^2} \sigma T^4. \tag{2.20}$$

For an archetypal NS with $M = 1.4 \; M_\odot$ and $R = 12$ km, with a temperature of $T = 10^{6.0}$ K, at a distance of 200 pc, this yields a value of

$F_{bolo} = 2.13 \times 10^{-10}$ erg/cm^2/s.

2.3 Flux From a Static NS in GR

Gravitational lensing will make a surface element appear larger, as demonstrated by Figure 2.4. An infinitesimal section of area on the NS surface as viewed by an observer at infinity can be described in terms of the impact parameter such that

$$dS_{obs} = b\ dbd\varrho \tag{2.21}$$

where ϱ describes rotation around the vector k (See Figure 2.4) (Pechenick et al., 1983a). The impact parameter is given by equation 2.4, and its derivative is simply

$$db = \frac{R\cos\alpha}{\sqrt{1-2M/R}}d\alpha. \tag{2.22}$$

The observed surface element is thus

$$dS_{obs} = \frac{R^2\cos\alpha}{1-2M/R}\sin\alpha\ d\alpha d\varrho, \tag{2.23}$$

or, since $\sin\alpha\ d\alpha = d\cos\alpha$,

$$dS_{obs} = \frac{R^2\cos\alpha}{1-2M/R}d\cos\alpha\ d\varrho. \tag{2.24}$$

The observed solid angle is subsequently

$$\begin{aligned} d\Omega_{obs} &= \frac{dS_{obs}}{d^2} \\ &= \frac{R^2}{d^2}\frac{\cos\alpha}{1-2M/R}d\cos\alpha\ d\varrho. \end{aligned} \tag{2.25}$$

Since the emission received by our detector will be redshifted due to the star's gravity—a phenomenon known as gravitational redshift—we must consider the

difference between the observed and emitted intensity in the GR case. The observed intensity is given by (Shu, 2010)

$$I_{E,obs} = \frac{I_{E,em}}{(1+z)^3}\eta, \tag{2.26}$$

where z is the gravitational redshift

$$\begin{aligned} z &= \frac{\Delta\lambda}{\lambda_{em}} \\ &= \frac{1}{(1-2M/R)^{1/2}} - 1, \end{aligned} \tag{2.27}$$

and η is the Doppler boosting term (discussed in section 2.4.1), which is just $\eta = 1$ for a static star. The emitted and observed energies are related by

$$E_{obs} = \frac{E_{em}}{1+z}, \tag{2.28}$$

where z is again the gravitational redshift. Making use of the relativistic transformation law for the specific intensity, the observed flux of photons with observed energy E_{obs} from a small surface element is

$$dF_{E,obs} = \frac{I_{E,em}}{(1+z)^3} d\Omega. \tag{2.29}$$

For the case of an isotropic, homogeneous NS with $i = 0°$, the spectral flux can be written

$$\begin{aligned} F_{E,em} &= \frac{R^2}{d^2}\int_0^{2\pi}\int_1^0 \frac{I_{E,em}}{(1+z)^3}\frac{\cos\alpha}{1-2M/R}\, d\cos\alpha\; d\varrho \\ &= \frac{R^2}{d^2}\int_0^{2\pi}\int_0^{\pi/2}\left(1-\frac{2M}{R}\right)^{1/2} I_{E,em}\cos\alpha\sin\alpha\; d\alpha\; d\varrho, \\ &= \frac{R^2}{d^2}\left(1-\frac{2M}{R}\right)^{1/2}\pi I_{E,em}, \end{aligned} \tag{2.30}$$

which is almost the same as the Newtonian expression for spectral flux, except for the additional gravitational redshift factor. Using the relationship between E_{obs} and E_{em} given by equation 2.28, we can set up the observed energy integral

$$\begin{aligned} F_{bolo} &= \frac{R^2}{d^2}\pi \int_0^\infty \frac{I_{E,em}}{(1+z)^3}\frac{dE_{em}}{1+z} \\ &= \frac{R^2}{d^2}\pi \left(1-\frac{2M}{R}\right)\int_0^\infty I_{E,em} dE_{em}. \end{aligned} \tag{2.31}$$

Integrating this as we did in 2.19, the observed bolometric flux in GR gives

$$F_{bolo} = \frac{R^2}{d^2}\left(1-\frac{2M}{R}\right)\frac{2\pi^5 k^4}{15c^2h^3}T^4. \tag{2.32}$$

Flux calculated using the Schwarzschild solution is thus related to its Newtonian equivalent by

$$F_{Sch} = \left(1-\frac{2M}{R}\right)F_{Newt}. \tag{2.33}$$

It is apparent that the GR flux $F_{Sch.}$ will always be less than the Newtonian flux $F_{Newt.}$; this is because although gravitational lensing increases the number of photons visible at infinity, gravitational redshift, which decreases the energy of photons leaving the surface of the NS, is the dominant effect.

For a real NS, the bending angle is not equal to the zenith angle ($\cos\Psi \neq \cos\alpha$). We can rewrite the solid angle in terms of the bending angle, Ψ, such that

$$d\Omega_{obs} = \frac{R^2}{d^2}\frac{\cos\alpha}{1-2M/R}\frac{d\cos\alpha}{d\cos\Psi}d\cos\Psi\ d\varrho. \tag{2.34}$$

We also want to define the solid angle with respect to the spin axis. For a spherically symmetrical object,

$$\begin{aligned} \sin\Psi\ d\Psi d\varrho &= \sin\theta\ d\theta d\phi \\ d\cos\Psi\ d\varrho &= \sin\theta\ d\theta d\phi, \end{aligned} \tag{2.35}$$

so the expression

$$d\Omega = \frac{R^2}{d^2}\frac{\cos\alpha\sin\theta}{1-2M/R}\frac{d\cos\alpha}{d\cos\Psi}d\theta d\phi \tag{2.36}$$

is geometrically equivalent. Allowing $\mu = \cos\alpha$ and $\zeta = \cos\Psi$, this becomes

$$d\Omega = \frac{R^2}{d^2}\frac{\mu\sin\theta}{1-2M/R}\frac{d\mu}{d\zeta}d\theta d\phi. \tag{2.37}$$

The bolometric flux can therefore be written

$$\begin{aligned} F_{bolo} &= \iint \frac{I_{E,em}}{(1+z)^4} d\Omega dE_{em} \\ &= \frac{R^2}{d^2}\iiint \frac{I_{E,em}}{(1+z)^4}\frac{\mu\sin\theta}{(1-2M/R)}\frac{d\mu}{d\zeta}d\theta d\phi dE_{em}, \end{aligned} \tag{2.38}$$

where the limits of integration are determined by the inclination angle i. Solving for μ given some value of ζ is accomplished using lookup tables, since solving equation 2.5 analytically is computationally intensive.

For the same archetypal NS described in the previous section, the bolometric flux will be $F_{bolo} = 1.41 \times 10^{-10}$ erg/cm^2/s using a relativistic model of gravity. For a spinning star, however, the degree of gravitational redshift will be dependent upon the location of the emission on the star, the angle of emission α, and the location of the observer relative to the spin axis. This is discussed in more detail in section 2.4.

2.4 Flux From a Rotating Star

2.4.1 Doppler Boosting

The fastest known spinning NS rotates at a speed of 716 Hz (Hessels et al., 2006). There is a large population of NSs spinning at a rate of 600 Hz (about 15% of the speed of light) (Lorimer, 2008; Papitto et al., 2014). For these rapidly spinning stars, Doppler effects must be taken into account to accurately determine the emitted flux. For high inclinations (where the spin axis $\hat{z}$ is nearly

orthogonal to the observer axis $\hat{k}$), light from the side of the star moving toward the observer will be blueshifted, while light on the other side will be redshifted. These frequency changes are what is generally meant when referring to the Doppler shifting of light. There is a second order effect, however, known as the transverse Doppler shift, which is non-negligible at low inclinations. For rapid motion perpendicular to the observer's line of sight, the wavelength of light from the surface appears larger due to disparate reference frames (the NS surface is travelling much more quickly than a comparatively static detector on Earth). This results in a slight redshifting of light from the surface. Both of these effects are contained in the Doppler boost function (Rindler, 1991)

$$\eta = \frac{\sqrt{1-v^2}}{1-v\cos\xi}, \tag{2.39}$$

where v is the linear speed of an arbitrary infinitesimal piece of the NS surface as a fraction of the speed of light, and ξ is the angle between the photon's initial direction in the frame of the observer and the photon's velocity vector (See Figure 2.5). Note that different sign conventions are used by different authors; in our notation, the velocity v is positive when the fluid is moving toward the observer.

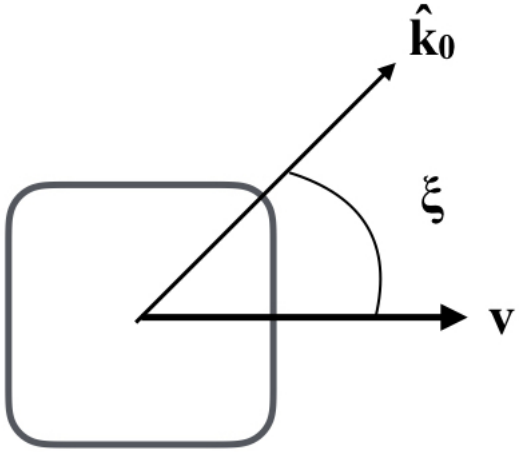

Figure 2.5: For some small area of surface on the NS, ξ describes the angle between the velocity vector and the direction of photon emission.

The speed v can be written (Morsink et al., 2007; Poutanen & Gierlinski, 2003)

$$v = \frac{2\pi\nu R \sin\theta}{\sqrt{1-2M/R}} \tag{2.40}$$

where ν is the frequency of the NS as measured by an observer on Earth (at infinity). The denominator represents the gravitational redshift, such that the speed is local to the NS. This has been defined explicitly in section 2.3. The cosine of the angle ξ is given by (Poutanen & Gierlinski, 2003)

$$\cos\xi = \frac{\sin\alpha \sin i \sin\phi}{\sin\psi}. \tag{2.41}$$

Implicit in this expression is the dependency of Doppler boosting on the phase angle ϕ, the inclination i, and the relationship between the zenith angles α and ψ. This geometry is shown in Figure 2.6. The α and ψ relationship is dependent on the mass and radius of the NS, so the degree of Doppler boosting may yield information about the star's compactness. To calculate the flux of a Doppler boosted star, we consider how rotation will shift the observed energies. Light emitted with energy E_{em} will be observed at energy E_{obs} (see equation 2.28). The Doppler shifted, observed energy is simply

$$E_{obs} = \frac{E_{em}}{1+z}\eta. \tag{2.42}$$

The conservation of specific intensity can be expressed

$$\frac{I_{obs}}{(E_{obs})^3} = \frac{I_{em}}{(E_{em})^3}, \tag{2.43}$$

so the Doppler boosted, observed intensity is

$$\begin{aligned} I_{obs} &= I_{em}\left(\frac{E_{obs}}{E_{em}}\right)^3 \\ &= I_{em}\left(\frac{\eta}{1+z}\right)^3. \end{aligned} \tag{2.44}$$

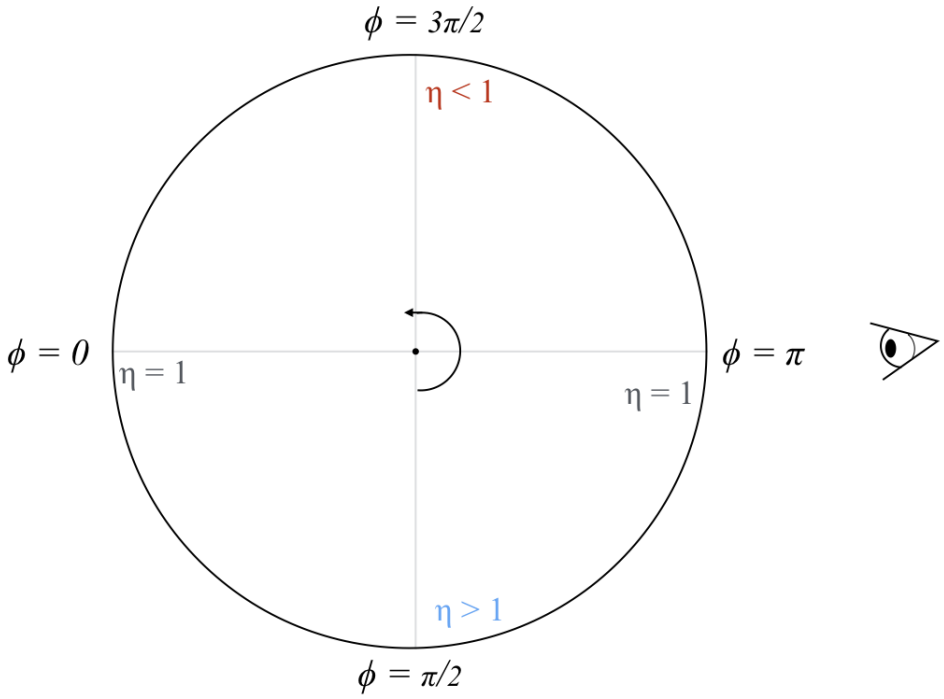

Figure 2.6: A visualization of the relationship between the azimuthal angle ϕ, the Doppler boost factor η, and the observer. When $\eta > 1$, the observer sees blueshifted light; when $\eta < 1$, she sees redshifted light.

Keeping this in terms of the Newtonian flux integral, the Doppler boosted, bolometric flux from a differential surface element can be written

$$dF_{Sch,Dopp} = \left(\frac{\eta}{1+z}\right)^3 \frac{\eta}{1+z} \frac{dF_{Newt}}{(1-2M/R)}, \tag{2.45}$$

where the first term comes from the intensity (equation 2.44), the second term comes from the observed energy (equation 2.42), and the final $1-2M/R$ comes from the solid angle. The Doppler boosted, bolometric flux from a differential surface element is thus

$$dF_{Sch,Dopp} = \eta^4 \left(1 - \frac{2M}{R}\right) dF_{Newt}. \tag{2.46}$$

The Doppler boost factor will change with both spin frequency and position on the star. Figure 2.7 demonstrates the latter by showing variation along

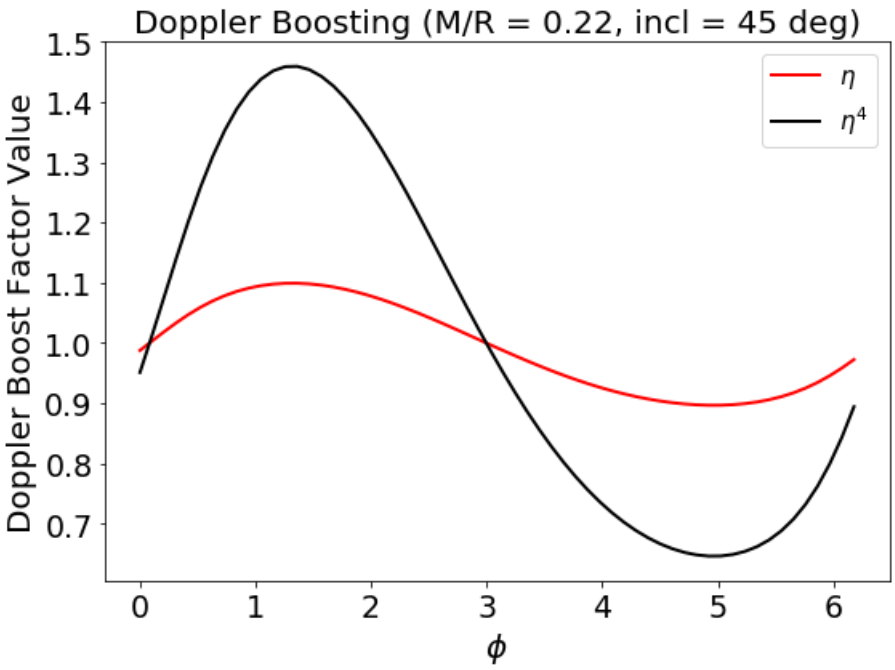

Figure 2.7: Doppler boost factor η and η^4 as a function of the azimuthal angle ϕ for a fixed θ value near the equator. Star is spherical and rotating at 600 Hz. Inclination is fixed at $i = 45°$ and compactness is fixed at $M/R = 0.22$.

the azimuthal angle ϕ. The curves peak near the edge of the star where the velocity vector is pointed directly at the observer; the trough is, likewise, where the vector is pointed directly away. For our archetypal NS with an inclination of $i = \pi/2$ with respect to the spin axis, this yields a value of $F = 1.43 \times 10^{-10}\text{erg/cm}^2\text{/s}$ for a spin frequency of 600 Hz, which is slightly larger than our unboosted GR flux. For an inclination of $i = 0$, the flux becomes $F = 1.36 \times 10^{-10}\text{erg/cm}^2\text{/s}$ for the same spin frequency. This value is smaller than the flux from a stationary star in GR ($1.41 \times 10^{-10}\text{erg/cm}^2\text{/s}$). This decrease occurs because, at low inclinations, the motion of the NS is orthogonal to the line of sight; relative to the observer, the time between successive light wave crests will appear to be dilated due to the transverse Doppler effect.

It is interesting to note that, because of the relationship between observed intensity and photon energy, a photon with a larger energy (and therefore a higher frequency) will necessarily have a higher intensity. The blueshifted side

of a rapidly rotating object will thus appear brighter than the redshifted side. This has been observed many times—recently, the first ever image of a black hole (taken by the Event Horizon Telescope in 2019) demonstrates this effect via the BH accretion disk, which is clearly brighter on one side (See Figure 2.8) (Akiyama et al., 2019). Cadeau et al. (2007) note that the asymmetry in the light curve due to Doppler boosting can be used to measure the velocity v; if the spin frequency is known, this provides one method of measuring the NS radius R.

Figure 2.8: Image of the shadow of the black hole M87 taken by the Event Horizon Telescope in 2019 (Akiyama et al., 2019). The lower half appears brighter due to Doppler boosting.

2.4.2 Oblateness

A rapidly rotating NS is not perfectly spherical. The more rapidly a NS is rotating, the more oblate it becomes—its equatorial radius grows significantly larger than its radius as measured from the centre to the pole. This has noticeable effects on the measured flux, particularly for very rapidly rotating stars (Morsink et al., 2007). A light curve simulation code, based on theory described

in Poutanen & Gierlinski (2003), is used to calculate the solid angle of oblate stars. This code is described in more detail in section 3.1.

For an oblate NS, the radial vector at a given location on the surface is different from the normal vector at the same location. We therefore define an oblate zenith angle β so that

$$\cos\beta = \hat{k_0} \cdot \hat{n}, \tag{2.47}$$

where $\hat{n}$ is the normal vector at the surface and $\hat{k_0}$ is the direction of emission (See Figure 2.9). The solid angle is therefore

$$d\Omega = \frac{R^2}{d^2} \frac{\sin\theta\cos\beta}{1-2M/R} \frac{d\cos\beta}{d\cos\Psi} d\theta d\phi, \tag{2.48}$$

which is the same as the solid angle in the spherical case, with the new angle $\cos\beta$ in place of $\cos\alpha$. Because the star's radius is now a function of θ, the value of the radius R and the surface gravity g must be calculated at each location on the star. The empirically derived equations used in these calculations are taken from AlGendy & Morsink (2014). Values of $\cos\beta$ are generated by the light curve simulation code flux-angles.

To determine the light curve of a star in general relativity, one must first describe the shape of the gravitational field outside the compact object. This takes the form of a solution to the Einstein field equations, also known as the metric. After the metric has been defined, the paths of the photons in spacetime (also known as geodesics) can be computed. For nonrotating stars, the Schwarzschild metric is sufficient (Pechenick et al., 1983b). This metric is given by

$$ds^2 = -\left(1-\frac{2M}{r}\right)dt^2 + \left(1-\frac{2M}{r}\right)^{-1} dr^2 + r^2(d\theta^2 + \sin^2\theta d\phi^2), \tag{2.49}$$

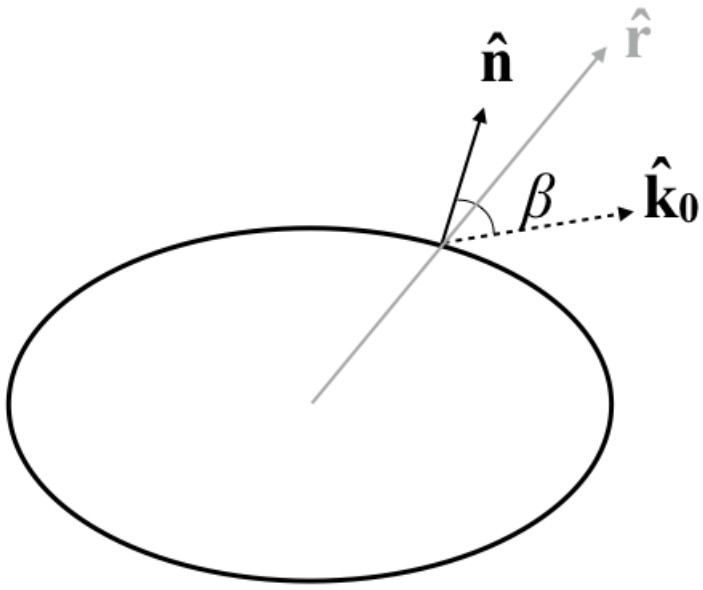

Figure 2.9: For an oblate NS, the radial vector $\hat{r}$ and normal vector $\hat{n}$ are not the same.

where $G = c = 1$ and $r = R(\theta)$. For slowly (< 300 Hz) rotating stars, the most common metric used for compact objects is the Schwarzschild-Doppler (S + D) approximation (Miller & Lamb, 1998; Poutanen & Gierlinski, 2003). The S + D approximation uses the Schwarzschild metric, then adds the Doppler terms as if the star were a rotating object with no gravitational field. This method was found to be inadequate for rapidly rotating stars, however; the increasingly oblate NS surface alters the direction in which photons are scattered, such that some locations on the NS surface which are invisible for a spherical star become visible for an oblate star, and vice versa. Morsink et al. (2007) developed the Oblate Schwarzschild (OS) approximation to resolve this discrepancy. It is the OS approximation which is used in our simulation of NS light curves.

We have used a great many angles in this chapter, and we will use many of them throughout this thesis. For ease of reference, each angle has been catalogued in Table 2.1.

Angle	**Definition**	**First Shown**
i	inclination angle	Figure 2.3
θ	polar angle	Figure 2.1
ϕ	azimuthal angle	Figure 2.1
α	zenith angle (spherical)	Figure 2.3
β	zenith angle (oblate)	Figure 2.9
μ	$\cos\alpha$ (spherical) or $\cos\beta$ (oblate)	
ξ	angle between velocity vector & direction of photon emission	Figure 2.5
Ψ	bending angle	Figure 2.3
ζ	$\cos\Psi$	
ϱ	rotation around $\hat{k}$	Figure 2.4

Table 2.1: Angles used in this thesis.

Chapter 3

Numerical Methods

3.1 flux-angles (C++ Code)

To begin with, the NS is divided into a grid of co-latitudes θ and azimuthal angles ϕ. It is necessary to specify the number of θ bins ($n\theta$) and ϕ bins ($n\phi$), as well as the NS mass, radius, spin frequency, surface temperature, inclination, and distance from the observer. Because θ is only defined for one hemisphere, it is prudent to double the ϕ bins so that $d\theta$ and $d\phi$ are the same size (e.g., if there are 10 θ bins there should be 20 ϕ bins). The star can be spherical or oblate. For each location on the NS surface, we must calculate the solid angle, photon emission angles, and Doppler boost value. This is accomplished using the C++ code flux-angles, which was developed using theoretical methods described in Poutanen & Gierlinski (2003) and Morsink et al. (2007). An earlier version of the code was used to compute light curves for oblate stars in Morsink et al. (2007); detailed documentation of this version of the code can be found on GitHub[1]. The relevant files generated by flux-angles are described in table 3.1.

[1] https://github.com/charleeamason/2019thesis

Example Filename	Contents
angles_sph_spin300_MR17_incl90.txt	θ coordinates, ϕ coordinates, cumulative value of $d\Omega$, size of θ bin ($d\theta$)
cosbeta_obl_spin600_MR17_incl0.txt	value of $\cos\beta$ for each (θ, ϕ).
dOmega_sph_spin0_MR22_incl30.txt	value of $d\Omega$ for each (θ, ϕ).
boost_obl_spin300_MR17_incl0.txt	value of Doppler boost (η) for each (θ, ϕ).

Table 3.1: Example output files produced for each run of the flux-angles program. The definitions of η, β, and $d\Omega$ are given by equations 2.39, 2.47, and 2.48, respectively.

'Sph' or 'obl' denotes whether the star is spherical or oblate; number after 'spin' denotes the spin frequency in Hz; number after 'MR' denotes the compactness, rounded to two decimal places and multiplied by 100; number after 'incl' denotes the inclination in degrees.

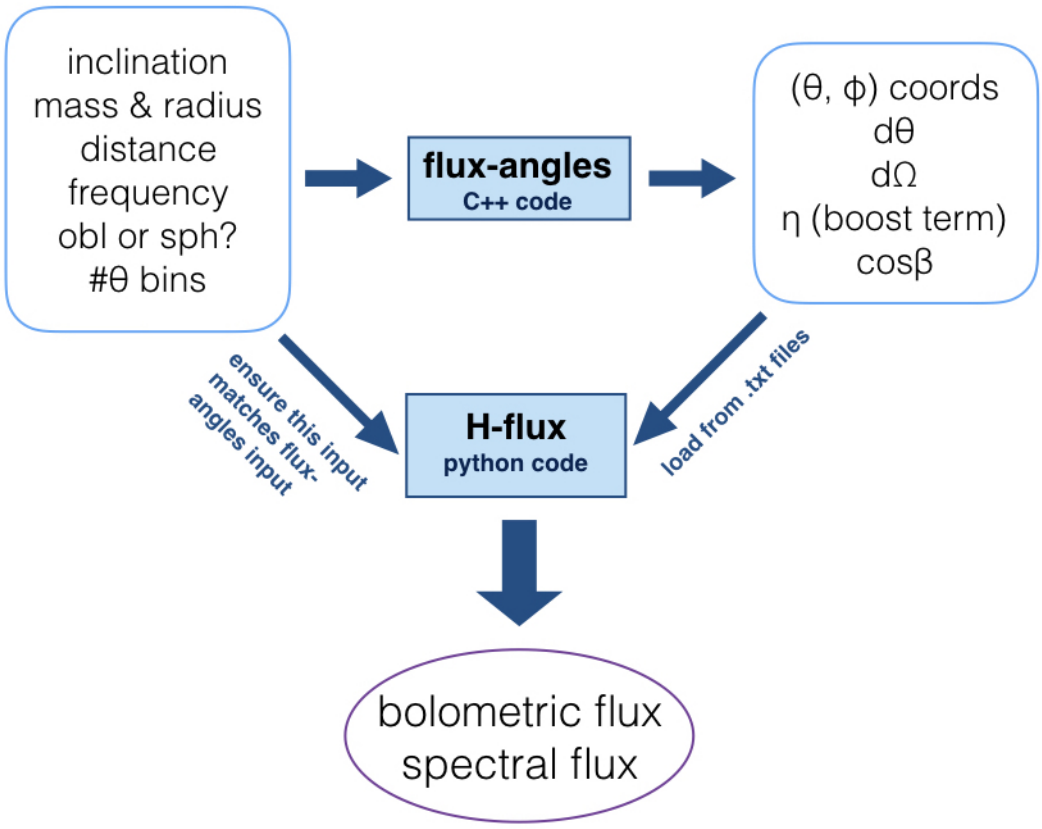

Figure 3.1: Flowchart describing the process by which we obtain the spectral and bolometric fluxes using the flux-angles C++ code and H-flux python code. In the spherical case $\cos\beta = \cos\alpha$. The H-flux algorithm is described in detail in figure 3.2.

3.2 H-flux (Python Code)

The python functions which calculate the spectral and bolometric fluxes are located in flux_GR_oblate.py, flux_GR_sphere.py, and flux_Newton.py. Each file contains two functions: one which determines the flux for a NS using a simple blackbody (get_flux_BB), and another (get_flux_H) which uses hydrogen atmosphere tables from Ho et al. (private communication, 2018). As these tables use fixed values of temperature T and gravitational acceleration g, it was necessary to write an interpolation function so that the hydrogen atmosphere model could be applied to NSs with a range of temperatures and gravitational accelerations. In the tables, specific intensity is normalized by the temperature cubed (I_ν/T^3) and evaluated for E/kT; to facilitate easier interpolation, we converted all of our energies to these dimensionless units. The structure of our interpolation algorithm is discussed in 3.3.7. For oblate stars, it is necessary to calculate the radius and gravitational acceleration at each point on the NS. This is accomplished using the programs get_R_theta.py and get_g.py, respectively.

To determine which function is appropriate, the input described in Figure 3.1 is required. This input will determine which text files from flux-angles will be called upon in the function. If the relevant flux-angles files have not been generated yet, the code will not run, so it is advisable to run the flux-angles code for all desired inclinations, spin frequencies, etc. before running the python code.

Due to the structure of the interpolation algorithm, the length of the energy list must match the number of photon energies in the hydrogen tables; as the tables from Wynn Ho et al. use 166 energies, our energy list has 166 entries. (Note these do not have to be the exact same energies, but the length of the lists must be the same.) Substituting 166 for the length of an alternative atmosphere model file should allow the use of models with different numbers

of photon energies.

Though the flux-angles code must run one inclination at a time, the H-flux python code allows for an inclination array of any length. The default is set to five inclinations $(0°, 30°, 45°, 60°, 90°)$. Inclinations less than $0°$ and greater than $90°$ will trigger an error due to the limitations of the numpy arccos function, but this is not an issue due to the symmetrical nature of the hemispheres of both spherical and oblate stars.

The files generated by H-flux will automatically be saved into a folder named ntheta# where '#' is the number of θ bins (e.g. ntheta30 for 30 θ bins). The names and contents of the output files are described in more detail in table 3.2. The overall structure of the H-flux code is outlined in Figure 3.2.

The data used in this research was generated with a 1.16 GHz Intel Core m^3 processor. For a single inclination in the simplest GR case (spherical, blackbody), our code takes on the order of minutes to run. For the most complicated GR case (oblate, H atmosphere), a single inclination takes many hours. Interpolating from the Ho tables is the most time consuming part of this process, and the interpolation algorithm could certainly be optimized. A faster processor would also ameliorate run times.

Example Filename	**Contents (by column)**
BB_bolo_newt_MR17_incl0.npz	1: Photon Energies (E/kT)
BB_spectra_obl_spin300_MR22_incl30.npz	2: Spectral Flux (erg/cm^2/s)
H_spectra_sph_spin0_MR17_incl45.npz	3: Spectral Intensity (erg/cm^2)

Table 3.2: Example output files produced for each run of H-flux. Each file contains the same 3 columns of information. Format is .npz, which is used for numpy arrays.

'BB' or 'H' denotes whether the flux is from a blackbody or hydrogen atmosphere; 'bolo' or 'spectra' denotes whether the file contains the bolometric or spectral flux; 'obl' or 'sph' denotes whether the star is oblate or spherical (not included for Newtonian model, which is only spherical); the number after 'spin' denotes the spin frequency in Hz (also not included for Newtonian model); the number after 'MR' denotes the compactness, rounded to two decimal places and multiplied by 100; the number after 'incl' denotes the inclination in degrees.

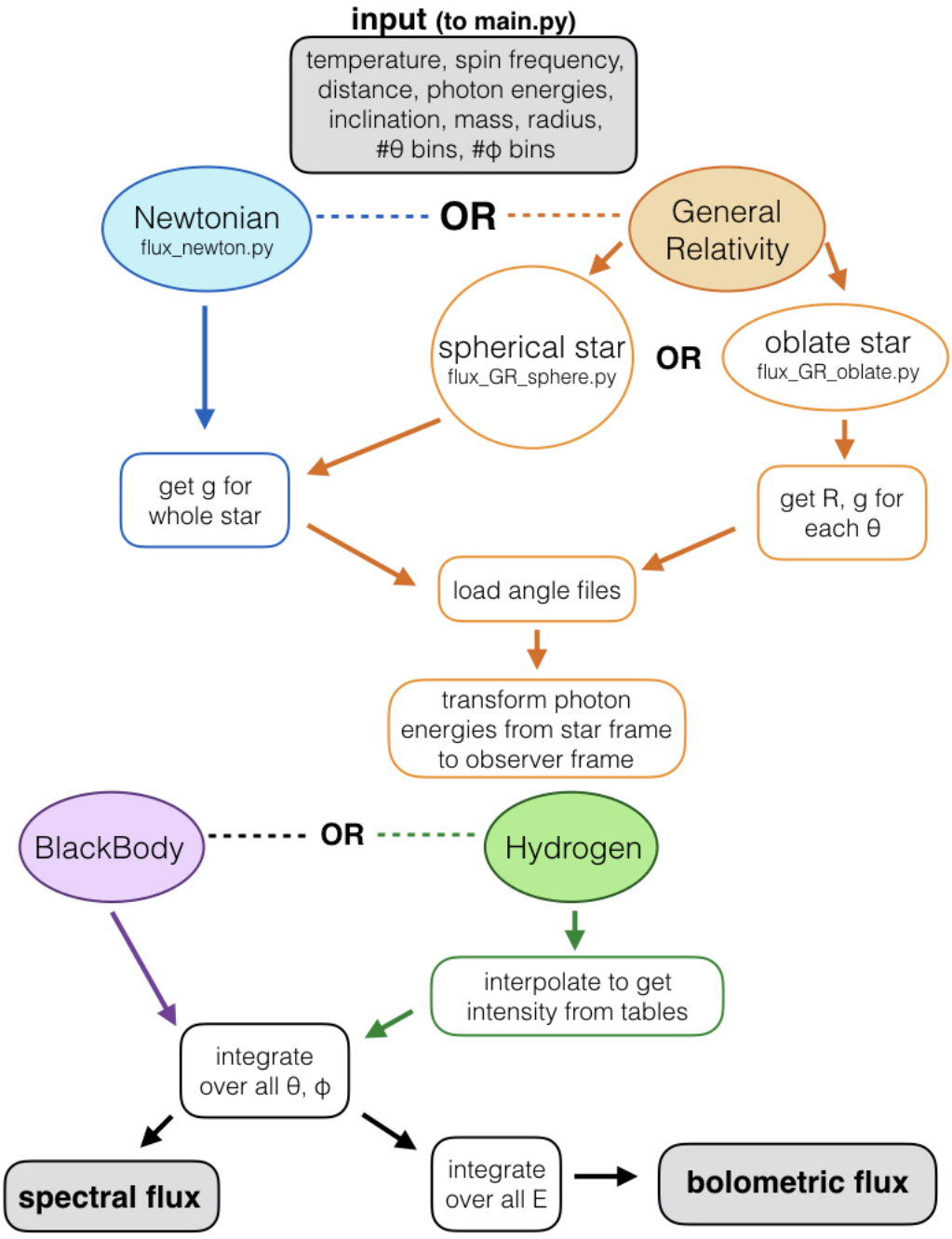

Figure 3.2: Description of the H-flux python code.

3.3 Interpolation Algorithm

Due to the variety of input used when calculating the flux—some arrays are evenly spaced, some are not—it was prudent to use more than one function to accomplish linear interpolation. Each of these functions contained in the master interpolation file interp_g_T_zeta.py is described in this section.

3.3.1 find_closest and get_nearest_pair

The function find_closest finds the closest value given a pair of test values and a target value. The function get_nearest_pair returns the two integers closest to a target integer in an array. The spacing between integers must be even for this function; this limitation was fine for the evenly spaced temperature and gravitational acceleration arrays, but for other parameters a function capable of dealing with unevenly spaced arrays was needed. Both find_closest and get_nearest_pair were modified from code found on stackexchange [2].

3.3.2 get_nearest_uneven

This function finds the closest pair of values in an array to a given target value. The array does not need to be evenly spaced. (The function get_nearest_pair is slightly faster, and is therefore still preferred for evenly spaced arrays.) If the target value is larger than any in the array, the pair of numbers returned will both be the maximum value in the array. If the target value is smaller than any in the array, the pair of numbers will, likewise, both be the minimum value in the array.

[2] https://codereview.stackexchange.com/questions/190145/find-the-closest-number-in-a-sorted-list-to-a-given-target-number/190180#190180

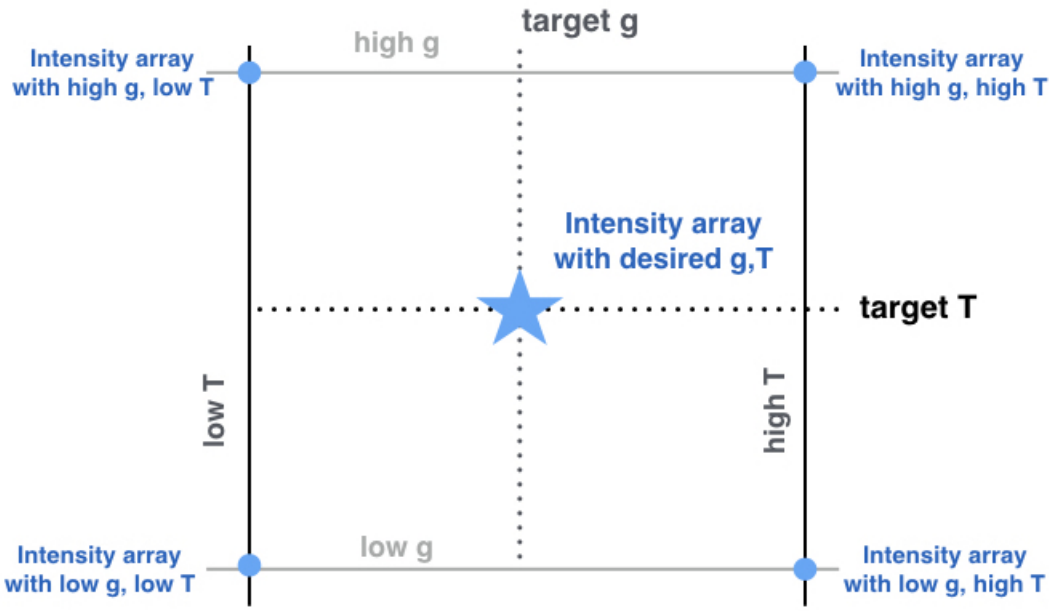

Figure 3.3: Two iterations of linear interpolation are required to get the desired intensity array.

3.3.3 interp_T_and_g

Since the temperature and gravitational acceleration arrays from Ho et al. are evenly spaced, interp_T_and_g makes use of the get_nearest_pair function to accomplish simple linear interpolation. The hydrogen tables have previously been divided into text files based on temperature and stored as '/logT_files/logT_#.txt' where '#' is the logT value multiplied by 100 (e.g., a temperature 10^6 K yields a filename logT_600.txt). The closest temperature values are selected based on the number in this filename. The data is then divided into arrays as shown in Figure 3.3 and linearly interpolated twice to get the intensity array associated with the target temperature and gravitational acceleration.

3.3.4 interp_zeta

This function interpolates the angle $\zeta = \cos\Psi (= \cos\alpha)$ in the Newtonian case, or $\mu = \cos\alpha$ in the GR case, such that it matches the angles given by the tables

in Ho et al. To make matters more confusing, this angle is called $\mu = \cos\theta$ in the Ho table README file, where Ho et al. define θ in the same way we have defined α. The function interp_zeta takes the output of interp_T_and_g as input, and returns the intensity and energy array with properly interpolated angles.

3.3.5 interp_E

This function is the final step in acquiring the spectral intensity for a NS with a hydrogen atmosphere. The energy list defined in main.py is interpolated using get_nearest_uneven and the photon energies in Ho et al. The final intensity array is returned.

3.3.6 lookup_alpha

A preliminary version of lookup_alpha_MR which assumed that the exact value of compactness was in the lookup table.

3.3.7 lookup_alpha_MR

Before the $\cos\beta$ angles were taken from flux-angles, it was necessary to use lookup tables (lookup_alpha.txt) to get the proper $\beta(=\alpha)$ values for an oblate star. This function is capable of reading in any M/R value and ζ value and returning $\alpha(=\beta)$ and $d\mu/d\zeta$. As reading in the flux-angles text files is faster than interpolating each angle one at a time, this function is not in use for the final version of our code.

Chapter 4

Results

4.1 Error and Convergence

To test the accuracy of our code, it is necessary to ensure the calculated flux converges to the correct value. For the blackbody model, this is straightforward, since the theoretical value can be determined analytically (as described in chapter 2). The percent error is simply calculated using

$$\%Error_{BB} = \frac{|\text{code value} - \text{theoretical value}|}{\text{theoretical value}} \times 100. \tag{4.1}$$

The convergence of the blackbody model with decreasing stepsize is catalogued in tables 4.1 and 4.2. Figure 4.1 shows how both the blackbody and H atmosphere bolometric flux behaves in Newtonian gravity; the error for the H model is on par with the blackbody model, with the inclination $i = 0°$ having the highest error and $i = 90°$ having the smallest error for both models. We think the $i = 0°$ error is disproportionately large because of the way the grid is defined, resulting in higher computational error near the poles. Using a different grid, or a different method of dividing up the NS surface, may alleviate this issue.

Figure 4.2 shows how the blackbody model behaves in general relativity. It

is interesting that the Newtonian flux varies with inclination considerably more than the GR flux. We are unsure why this is so.

Determining error for the H atmosphere model is somewhat more complicated, because the theoretical flux value is unknown. Flux should be constant at all inclinations for a spherical star, however; we use this fact to estimate error for the H model. The percent error is thus the flux range over the inclination averaged flux, i.e.,

$$\%Error_H = \frac{|F_{incl=90} - F_{incl=0}|}{F_{avg}} \times 100. \tag{4.2}$$

Figure 4.3 shows both blackbody and H models at different resolutions in general relativity. In GR, the blackbody error is considerably lower than the H atmosphere error, with percent error on order of 0.18% for the blackbody at $n\theta = 120$, and 0.4% for the H atmosphere at the same resolution. For all error calculations a NS with $M = 1.4\ M_\odot$, $R = 9.37$ km, and $T = 10^{6.0}$ K, at a distance of 200 pc, is used. We use this atypically small value of R because it yields a more typical value of compactness ($M/R = 0.22$) than $R = 12$ km ($M/R = 0.17$) for $M = 1.4\ M_\odot$. This is necessary since we are keeping the mass fixed; a real NS with a this compactness would have a higher mass.

It is important to compare the size of our error with the expected size of the effects we are measuring. Spin effects can change observed flux by $1-12\%$, depending on the size of the NS, the inclination of the observer, and the magnitude of the spin frequency (Baubock et al., 2015). H atmospheres do not significantly change the bolometric flux when compared to a blackbody model, but the change in the spectral flux can impact inferred radii measurements by a factor of 3 (Zavlin et al., 2002) (see Figure 4.4).

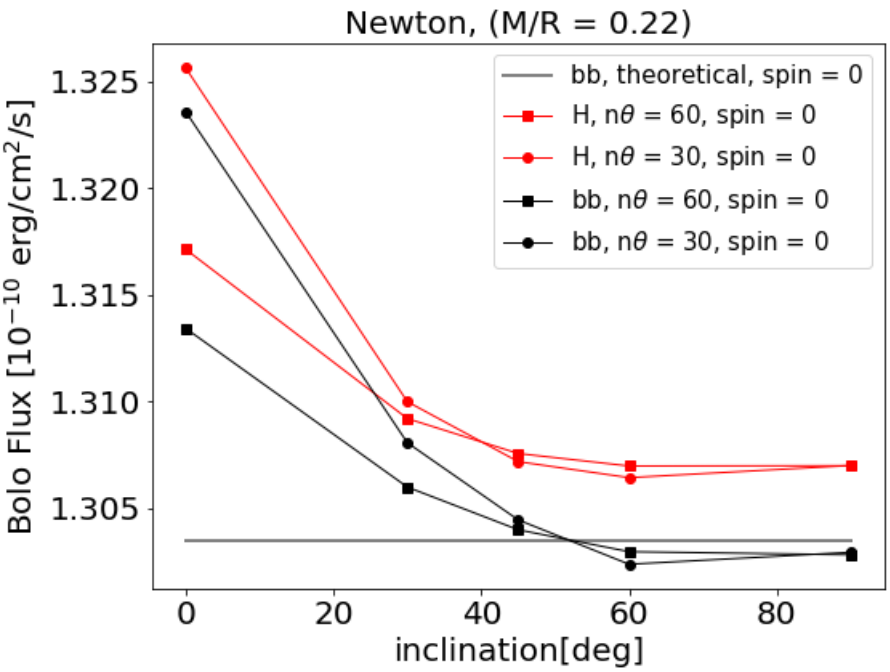

Figure 4.1: Bolometric fluxes for different resolutions (values of $n\theta$). Percent error measured at $i = 0°$ is on order of 1.5% for the blackbody model with $n\theta = 30$, 0.8% for the blackbody model with $n\theta = 60$, 1.4% for the H model with $n\theta = 30$, and 0.8% for the H model with $n\theta = 60$.

Incl.(deg)	Flux (erg/cm^2/s), $n\theta = 10$	% Err.	Flux , $n\theta = 30$	% Err.
0	1.35741×10^{-10}	4.1%	1.32358×10^{-10}	1.54%
30	1.29735×10^{-10}	0.47%	1.30807×10^{-10}	0.35%
45	1.29652×10^{-10}	0.54%	1.30446×10^{-10}	0.074%
60	1.29333×10^{-10}	0.78%	1.30238×10^{-10}	0.086%
90	1.30428×10^{-10}	0.060%	1.30294×10^{-10}	0.043%

Table 4.1: Stationary Newtonian NS with blackbody surface. Observed bolometric converges toward the correct value with 30 θ bins.

Observed bolometric flux for a spherical, stationary NS under Newtonian gravity. The $n\theta$ and $n\phi$ describe the size of the θ and ϕ bins, respectively; the energy stepsize is held constant at $E_{dx} = 0.2$. Flux converges toward the correct value, 1.3035×10^{-10}erg/cm^2/s, with decreasing stepsize.

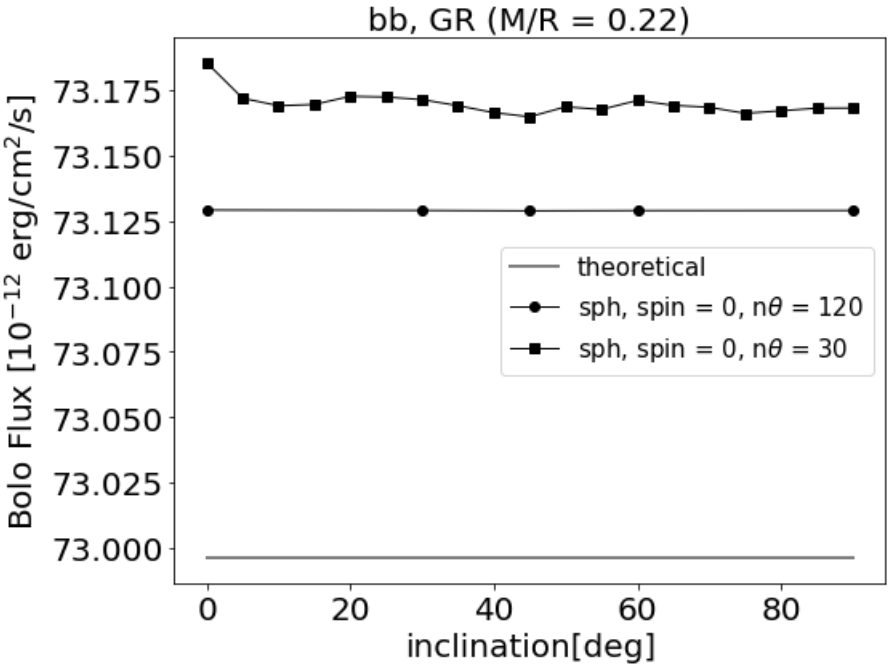

Figure 4.2: Bolometric fluxes for different resolutions (values of $n\theta$). Blackbody only. At $i = 0°$, percent error is on order 0.26% for the lower resolution and 0.18% for the higher resolution.

Incl. (deg)	Flux (erg/cm^2/s) $n\theta = 10$	% Err.	Flux (erg/cm^2/s) $n\theta = 30$	% Err.	Flux (erg/cm^2/s) $n\theta = 120$	% Err.
0	7.3387×10^{-11}	0.54%	7.3185×10^{-11}	0.26%	7.3129×10^{-11}	
30	7.3464×10^{-11}	0.64%	7.3171×10^{-11}	0.24%	7.3129×10^{-11}	
45	7.3432×10^{-11}	0.60%	7.3164×10^{-11}	0.23%	7.3129×10^{-11}	0.18%
60	7.3409×10^{-11}	0.57%	7.3171×10^{-11}	0.24%	7.3129×10^{-11}	
90	7.3435×10^{-11}	0.60%	7.3168×10^{-11}	0.24%	7.3129×10^{-11}	

Table 4.2: Stationary NS in GR with blackbody surface. Observed bolometric converges toward the correct value with 120 θ bins.

Observed bolometric flux for a spherical, stationary NS in general relativity. The $n\theta$ and $n\phi$ describe the size of the θ and ϕ bins, respectively; the energy stepsize is held constant at $E_{dx} = 0.2$. Flux converges toward the correct value, 7.2996×10^{-11}erg/cm^2/s, with decreasing stepsize.

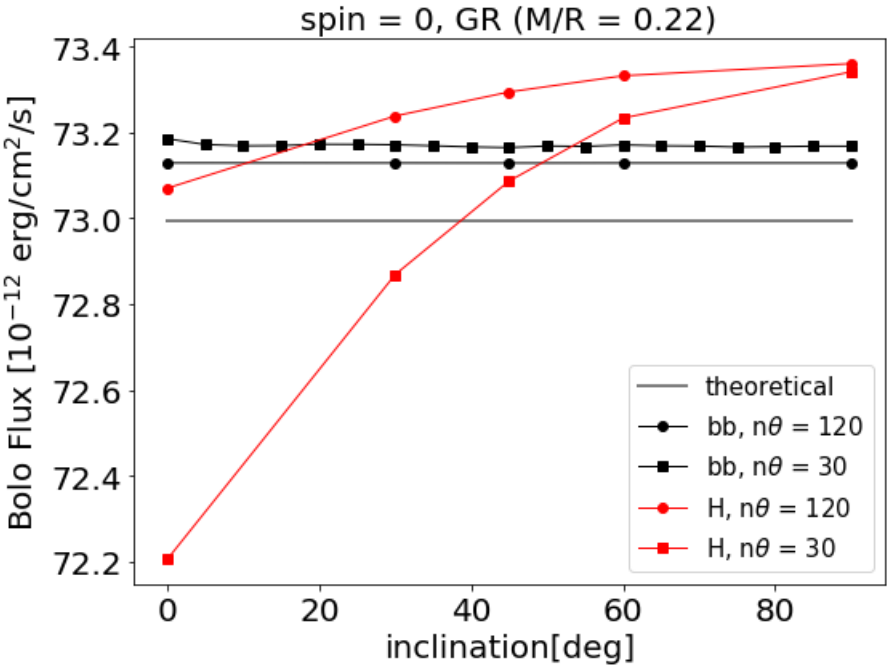

Figure 4.3: Bolometric fluxes for different resolutions (values of $n\theta$). Blackbody and H. For H atmosphere, percent error is on order 1.6% for the lower resolution and 0.4% for the higher resolution. Blackbody percent error is same as in Figure 4.2.

Incl. (deg)	Flux (erg/cm^2/s) $n\theta = 10$	% Err.	Flux (erg/cm^2/s) $n\theta = 30$	% Err.	Flux (erg/cm^2/s) $n\theta = 120$	% Err.
0	7.01535×10^{-11}		7.22065×10^{-11}		7.3070×10^{-11}	
30	7.20674×10^{-11}		7.28692×10^{-11}		7.3238×10^{-11}	
45	7.26810×10^{-11}	4.5%	7.30871×10^{-11}	1.6%	7.3294×10^{-11}	0.40%
60	7.30856×10^{-11}		7.32335×10^{-11}		7.3332×10^{-11}	
90	7.33872×10^{-11}		7.33412×10^{-11}		7.3360×10^{-11}	

Table 4.3: Stationary NS in GR with a H atmosphere. Observed bolometric starts to converge with 120 θ bins.

Observed bolometric flux for a spherical, stationary NS in general relativity. The $n\theta$ and $n\phi$ describe the size of the θ and ϕ bins, respectively; the energy stepsize is held constant at $E_{dx} = 0.2$. Percent error applies to all inclinations, not only $i = 45°$.

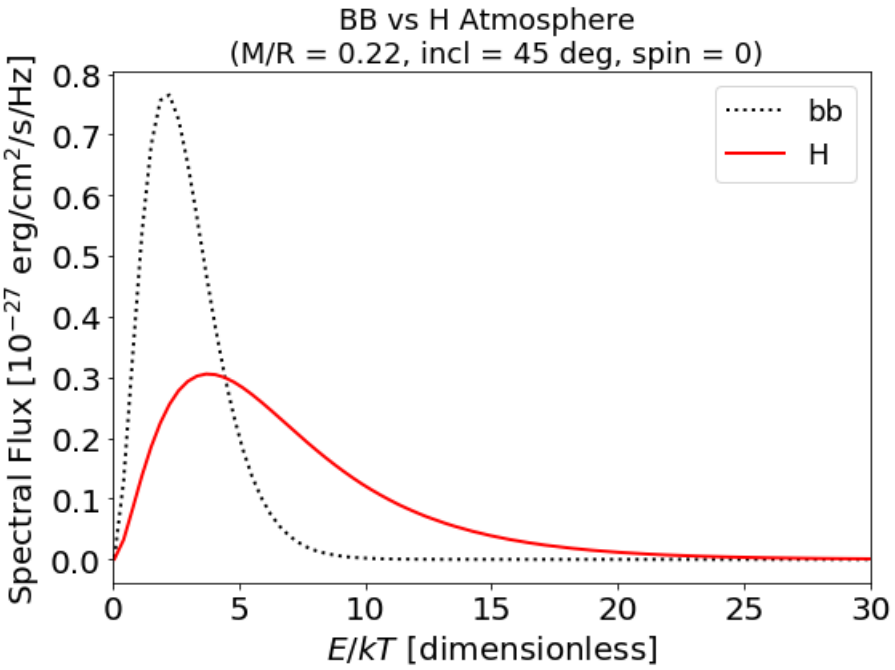

Figure 4.4: A blackbody compared to a hydrogen atmosphere model. The hydrogen atmosphere shifts the peak to higher frequencies.

4.2 General Relativistic Effects

The salient difference between GR and Newtonian gravity from a calculation standpoint is that for GR, $\psi \neq \alpha$. Calculating α analytically using equation 2.5 is computationally intensive; instead, we interpolate between values in a lookup table compiled by Sharon Morsink to determine the appropriate α (private communication, 2019). Calculated analytically for $i = 0°$, the bolometric flux is 7.2996×10^{-11}erg/cm^2/s for the archetypal NS described at the beginning of this chapter; the numerical integral begins to converge to this value regardless of inclination (see table 4.2). The GR and Newtonian fluxes are compared in Figure 4.5.

The range of each integral depends on which parts of the NS are visible, which in turn depends on the inclination i. Visibility conditions are calculated at each step such that only light the observer will see is added to the flux. The bolometric flux of a star with gravitational redshift is calculated using our numerical integrator for the same range of inclinations as in the previous section (e.g., $i = 0°, 30°, 45°, 60°, 90°$). These results are given in Table 4.2. Note that for Figure 4.4 and all subsequent blackbody spectral flux plots, the peak is located at approximately 3 E/kT units, or about 0.26 keV. The hydrogen atmosphere spectral flux peak is a bit higher energy than this. Both of these peak values are within the Chandra telescope's observing capabilities, which can detect light in the range $0.2 - 10$ keV[1].

[1]See https://chandra.harvard.edu/about/specs.html for Chandra specifications

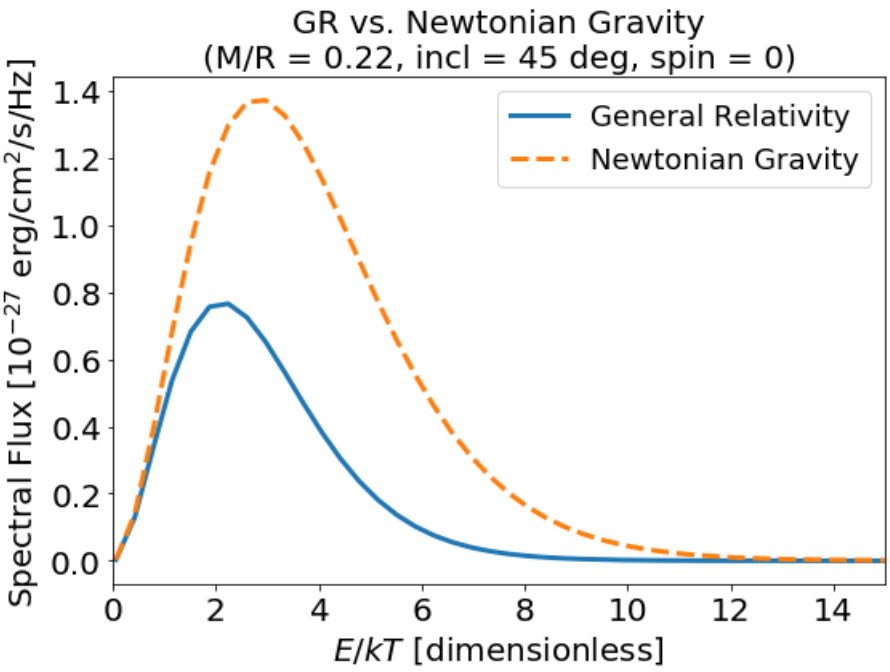

Figure 4.5: Static, blackbody NS with Newtonian gravity compared with the same NS in GR. Gravitational redshift results in less flux.

4.3 Effects of Compactness

The effect of compactness on flux can be seen in Figure 4.6. Three values of compactness are examined, with mass fixed at $M = 1.4\ M_\odot$. Higher compactness results in a smaller star, which in turn results in less flux. Though the radii used ($R = 12$ km for $M/R = 0.17$, $R = 9.37$ km for $M/R = 0.22$, and $R = 7.64$ km for $M/R = 0.27$), particularly the smallest radius $R = 7.64$ km, are not necessarily realistic for a $M = 1.4\ M_\odot$ star, it is the overall compactness value which we are concerned with, not the M and R values individually. A more realistic NS with a compactness $M/R = 0.27$ would have a higher mass and a radius closer to the archetypal value of 10 km; but the difficulty of determining the exact radius from M/R is part of what makes finding the NS EOS so difficult. It is important to keep this in mind when considering compactness.

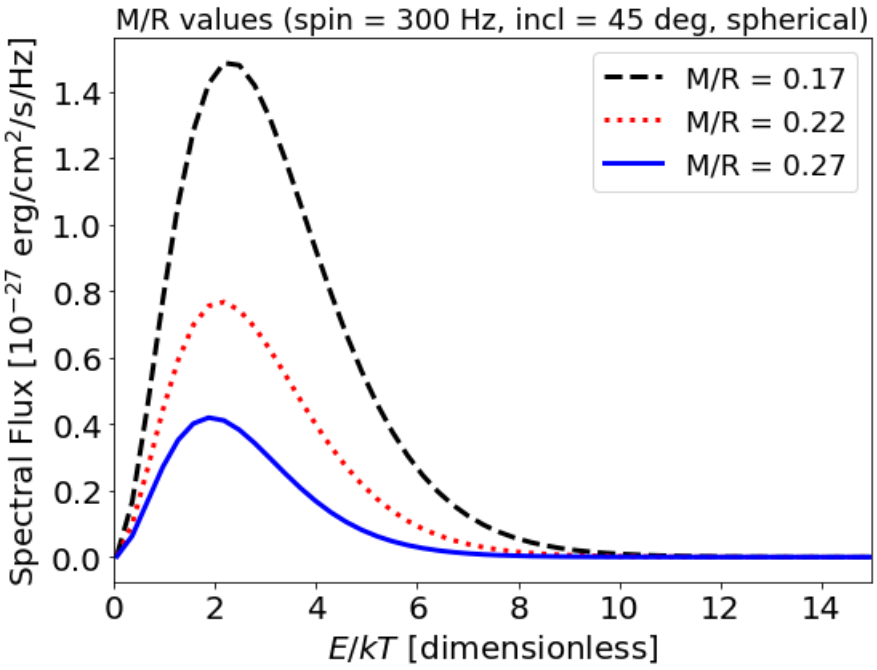

Figure 4.6: Spectral flux with different values of compactness for a spherical blackbody NS. Spin and inclination are fixed.

4.4 Spin Effects

The change in solid angle for different inclinations and two spin frequencies is shown in Figure 4.7. At high inclinations, a spinning star appears smaller compared to a static, spherical star with the same equatorial radius. This is because the cross-sectional area of an oblate star is smaller than that of a spherical star with the same equatorial radius. At low inclinations, a spinning star has similar surface area (or exactly the same surface area in the $i = 0°$ case) as a spherical star. The NS appears larger, however, since light bends differently around an oblate star compared to a static, spherical star (an observer can see a little further around the equator in the oblate case (Morsink et al., 2007)).

Figures 4.8 and 4.9 show how bolometric flux changes with inclination for a blackbody and H atmosphere model, respectively. Flux is plotted for two different spin values (300 and 600 Hz), and for oblate and spherical stars in both cases. Looking at the spherical, spinning stars in both plots, Doppler

effects are readily apparent; Doppler boosting at high inclinations results in more flux, while the transverse Doppler shift at low inclinations decreases flux. Adding oblateness to the equation, we see that flux dramatically decreases at high inclinations due to smaller surface area. At low inclinations, the spherical and oblate curves are similar (and nearly identical for the blackbody plot). Oblateness thus has the largest impact on flux at high inclinations. Note that, in the blackbody plot, there is a location (at $i = 25°$) where the spherical and oblate fluxes are the same for the 600 Hz case. As the blackbody and H atmosphere plots have similar overall behavior, it is likely that this feature is also present in the H atmosphere plot, but due to computational limitations, it is not currently resolvable.

Figures 4.10, 4.11, and 4.12 show spectral flux for a blackbody at different inclinations. For each of these plots, we include a residual plot so that differences between curves can be easily seen. Figure 4.10 shows a NS spinning at 300 Hz; for the three inclinations shown ($i = 0°, 45°, 90°$) the differences between spectral fluxes are negligible, with the $i = 45°$ case having only a 0.60% difference with the $i = 0°$ case, and the $i = 90°$ case having only a 0.74% difference with the $i = 0°$ case. This suggests that spin effects are negligible for stars spinning at this frequency. Figure 4.11 shows the same star as Figure 4.10, but spinning at a higher frequency (600 Hz). The inclination differences are more apparent here, with the $i = 45°$ case having a 1.87% difference compared to the $i = 0°$ case, and the $i = 90°$ case having a 2.29% difference compared to the $i = 0°$ case. These differences are small but potentially measurable by future instruments (e.g., by the Advanced Telescope for High-ENergy Astrophysics[2], abbreviated 'ATHENA'). Compared to Chandra, ATHENA will have an expanded range in both higher and lower energies, with the wide field imager capable of detecting emission in the range $0.1 - 15$ keV.

Figure 4.12 allows the comparison of spherical and oblate spectral fluxes

[2]http://sci.esa.int/athena/

at two inclinations. The two oblate curves are the same as on the previous plot (Figure 4.11), with the spherical NS now included for comparison. Note that the two spherical inclinations are nearly identical, but the two oblate inclinations are different; this suggests that oblateness is of similar or greater importance compared to Doppler boosting. These results agree qualitatively with Baubock et al. (2015).

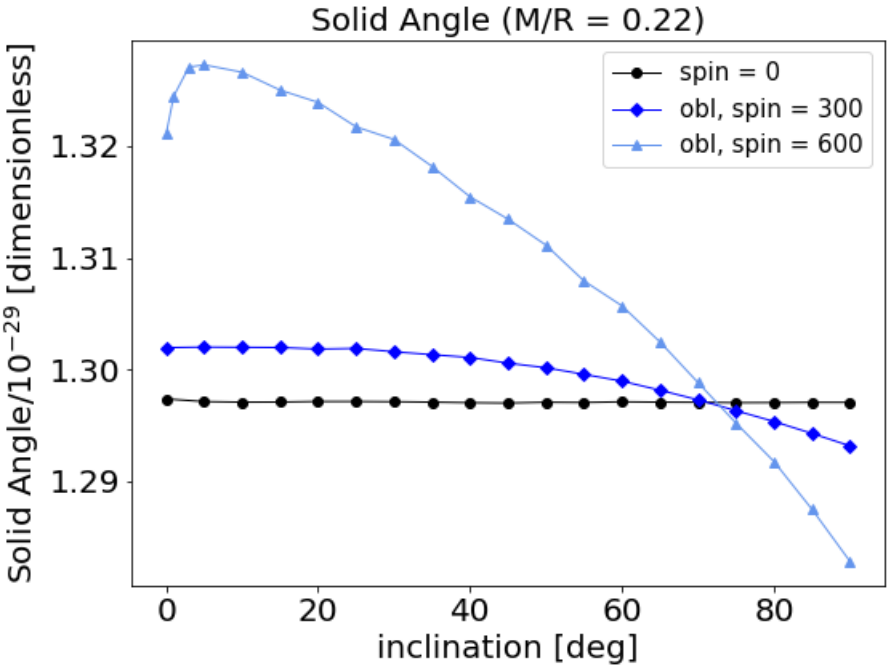

Figure 4.7: Change in solid angle for different inclinations. Stationary, spherical star shown for comparison.

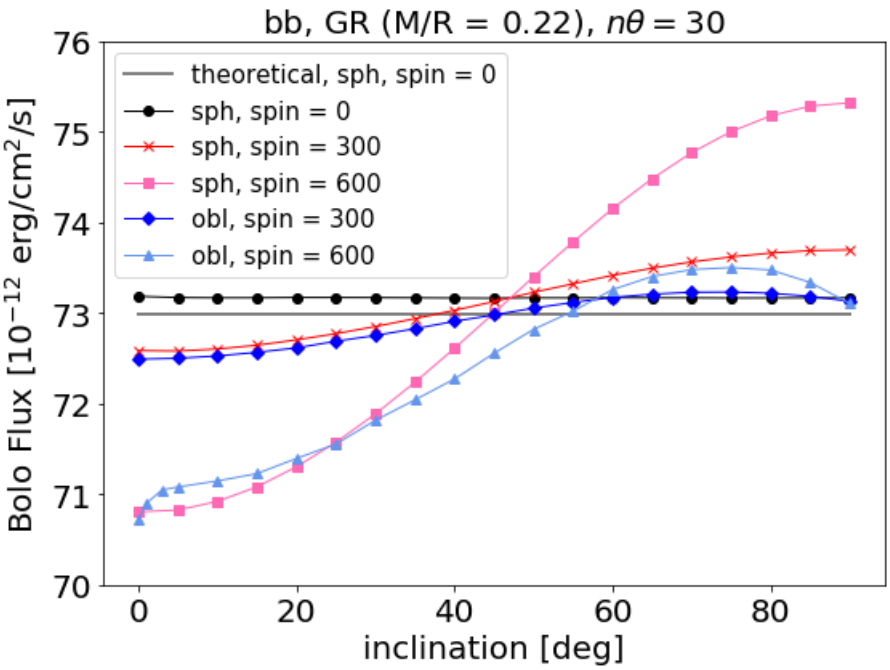

Figure 4.8: Bolometric flux produced by a blackbody NS (using 30 θ bins). Shape (spherical vs. oblate) and spin frequency is varied while compactness is held constant.

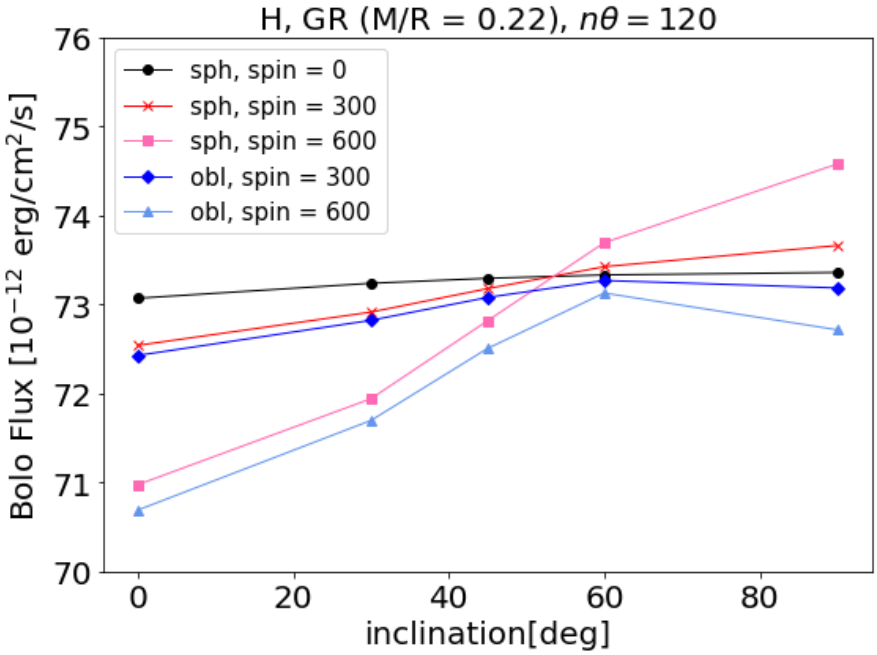

Figure 4.9: Bolometric flux produced by both spherical and oblate NSs with a H atmosphere (120 θ bins). Spin frequency is varied while compactness is held constant.

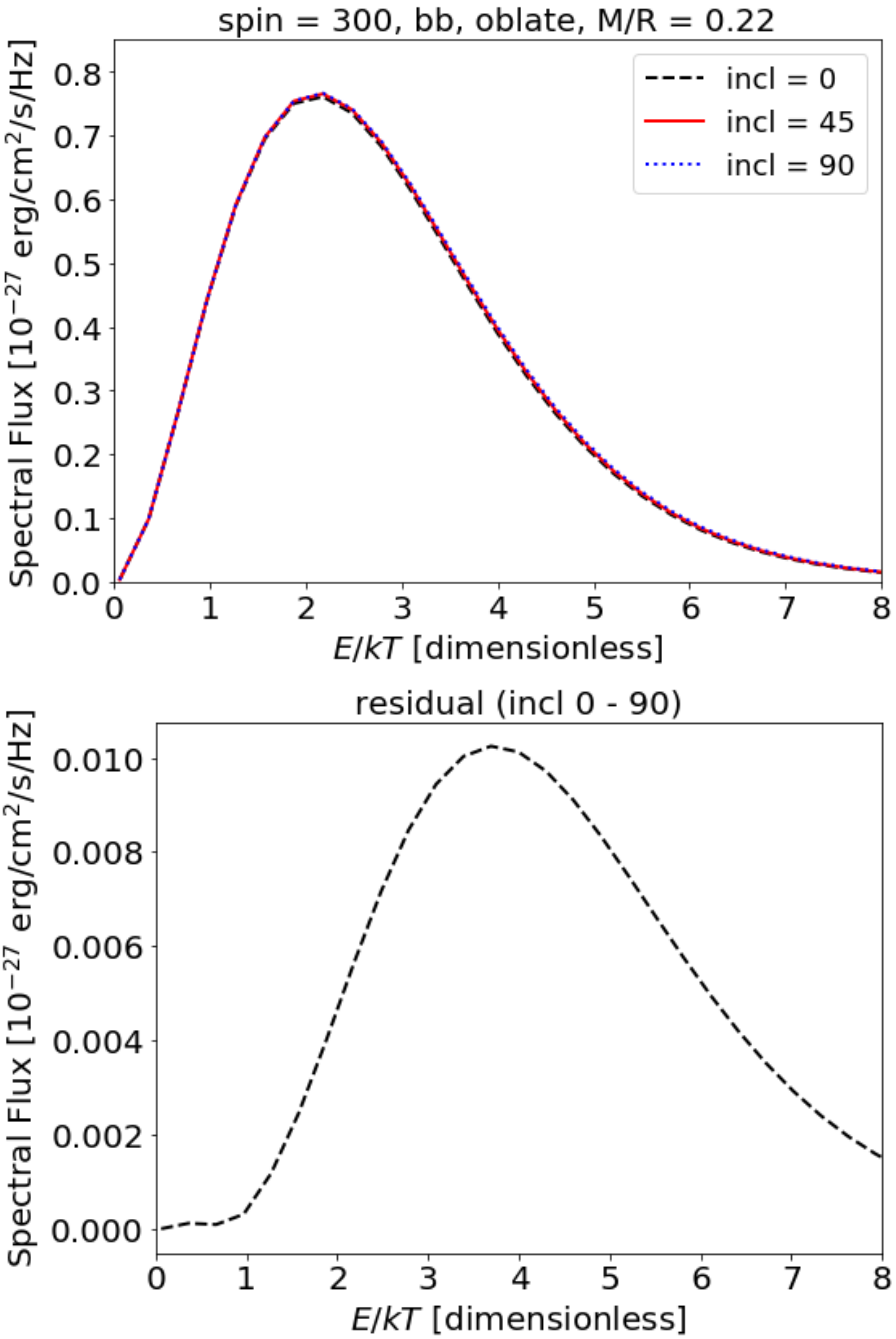

Figure 4.10: Top: Spectral flux at varying inclinations for an oblate NS using a blackbody model with spin fixed at 300 Hz ($n\theta = 30$). Differences are negligible at this spin frequency. Bottom: Difference between the $i = 0°$ and $i = 90°$ curves.

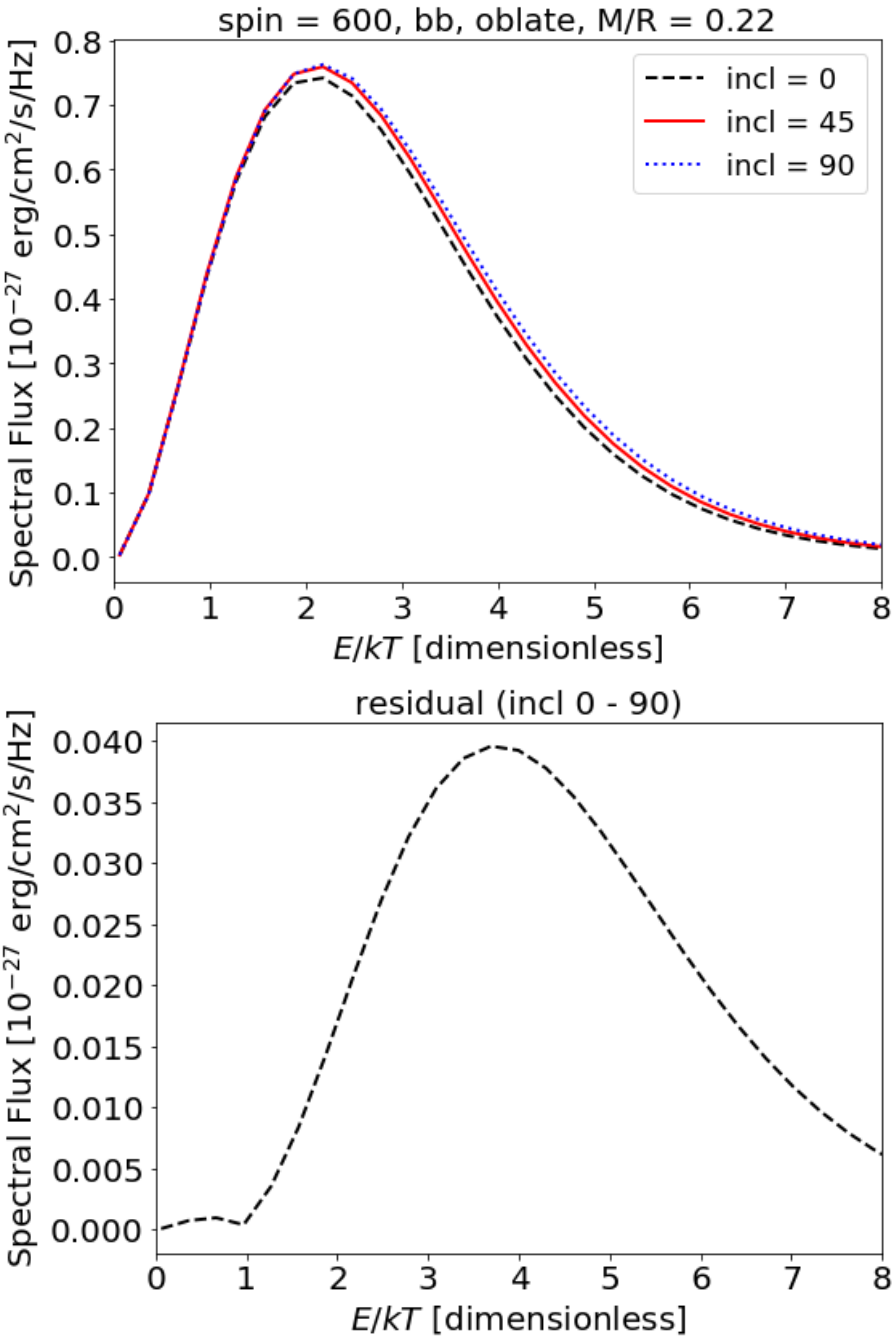

Figure 4.11: Top: Spectral flux at varying inclinations for an oblate NS using a blackbody model with spin fixed at 600 Hz ($n\theta = 30$). High inclinations ($i = 90°$) have larger observed fluxes than low inclinations ($i = 0°$). Bottom: Difference between the $i = 0°$ and $i = 90°$ curves.

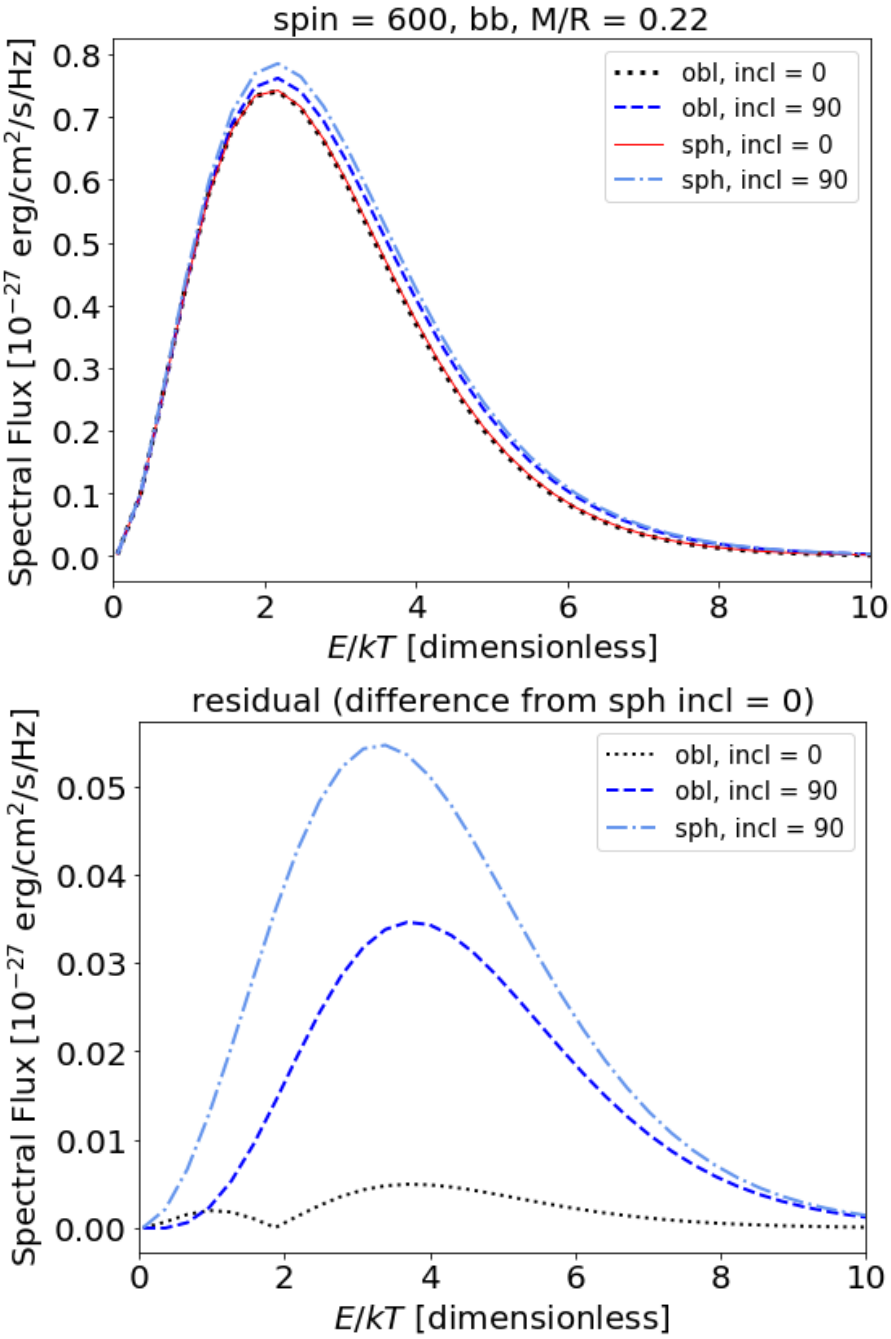

Figure 4.12: Top: Spectral flux at varying inclinations for both spherical and oblate NSs using a blackbody model with spin fixed at 600 Hz ($n\theta = 30$). High inclinations ($i = 90°$) have larger observed fluxes than low inclinations ($i = 0°$). For high inclinations, spherical stars have larger fluxes than oblate stars; they are nearly identical at low inclinations. Bottom: Difference as measured from the spherical $i = 0°$ curve.

4.5 Effects of Hydrogen Atmosphere

As anticipated, the H atmosphere model shifts the spectral flux to higher frequencies (again refer to Figure 4.4). Figures 4.13 and 4.14 show spectral flux for a H atmosphere model at different inclinations (with residuals again shown to highlight inclination difference). For a NS spinning at 300 Hz, an observer at $i = 45°$ will measure only a 1.87% difference compared with the $i = 0$ case; an observer at $i = 90°$ will measure a 2.29% difference. For a NS spinning at 600 Hz, these percent differences become 3.77% and 4.31%, respectively. These differences should be smaller with a hydrogen atmosphere, compared to a blackbody; H atmosphere emission is anisotropic due to electron scattering in the atmosphere (Rybicki & Lightman, 1979). This anisotropy causes increased limb darkening, which in turn reduces the effects of relativistic boosting and oblateness. However, the opposite seems to be happening, with the H atmosphere model having larger variation with inclination than the blackbody model. This is likely due to the larger error in the H atmosphere results. Higher grid resolution will enable us to determine whether error is the culprit, or if this is a real effect.

Like Figure 4.12, Figure 4.15 allows the comparison of spherical and oblate spectral fluxes at two inclinations. The two oblate curves are the same as in Figure 4.14, with the spherical NS now included for comparison. Note that, just as in the blackbody case, the two spherical inclinations are nearly identical, but the two oblate inclinations are quite different. Oblateness effects, though small, are still evident in the presence of a H atmosphere.

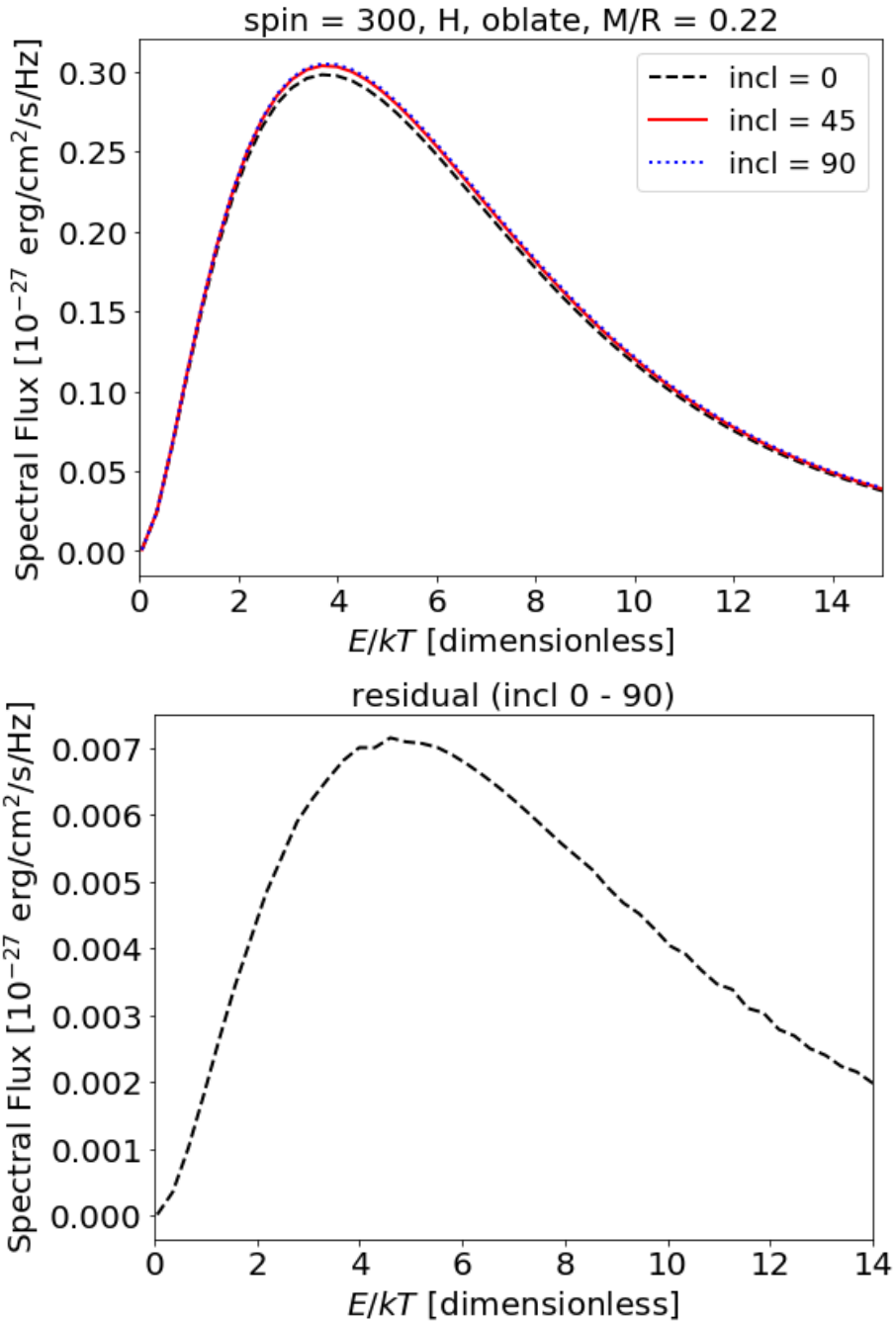

Figure 4.13: Top: Spectral flux at varying inclinations for an oblate NS using a hydrogen atmosphere model with spin fixed at 300 Hz ($n\theta = 30$). High inclinations ($i = 90°$) have larger observed fluxes than low inclinations ($i = 0°$). Bottom: Difference between the $i = 0°$ and $i = 90°$ curves.

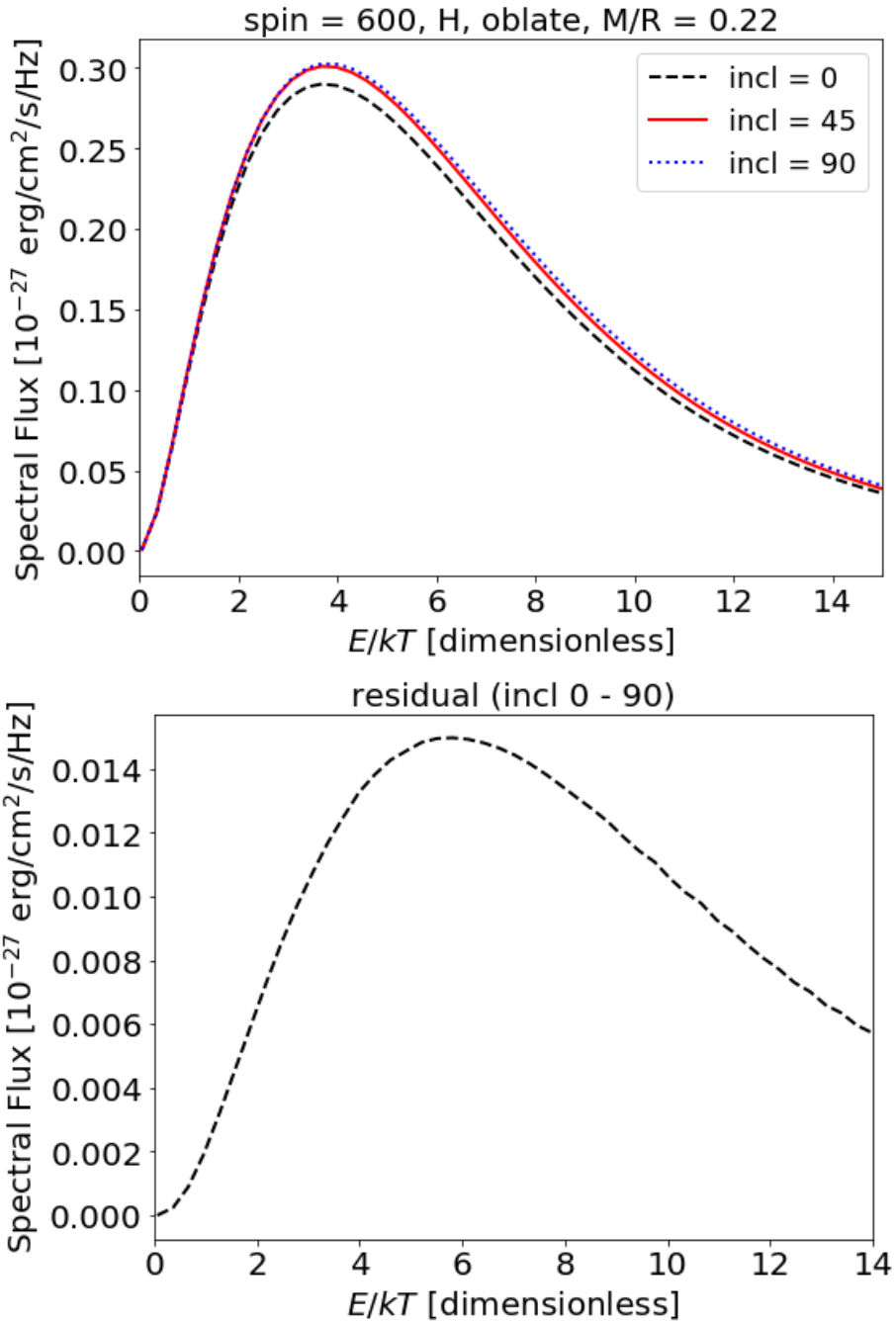

Figure 4.14: Top: Spectral flux at varying inclinations for an oblate NS using a hydrogen atmosphere model with spin fixed at 600 Hz ($n\theta = 30$). High inclinations ($i = 90$) have larger observed fluxes than low inclinations ($i = 0$). Bottom: Difference between the $i = 0°$ and $i = 90°$ curves.

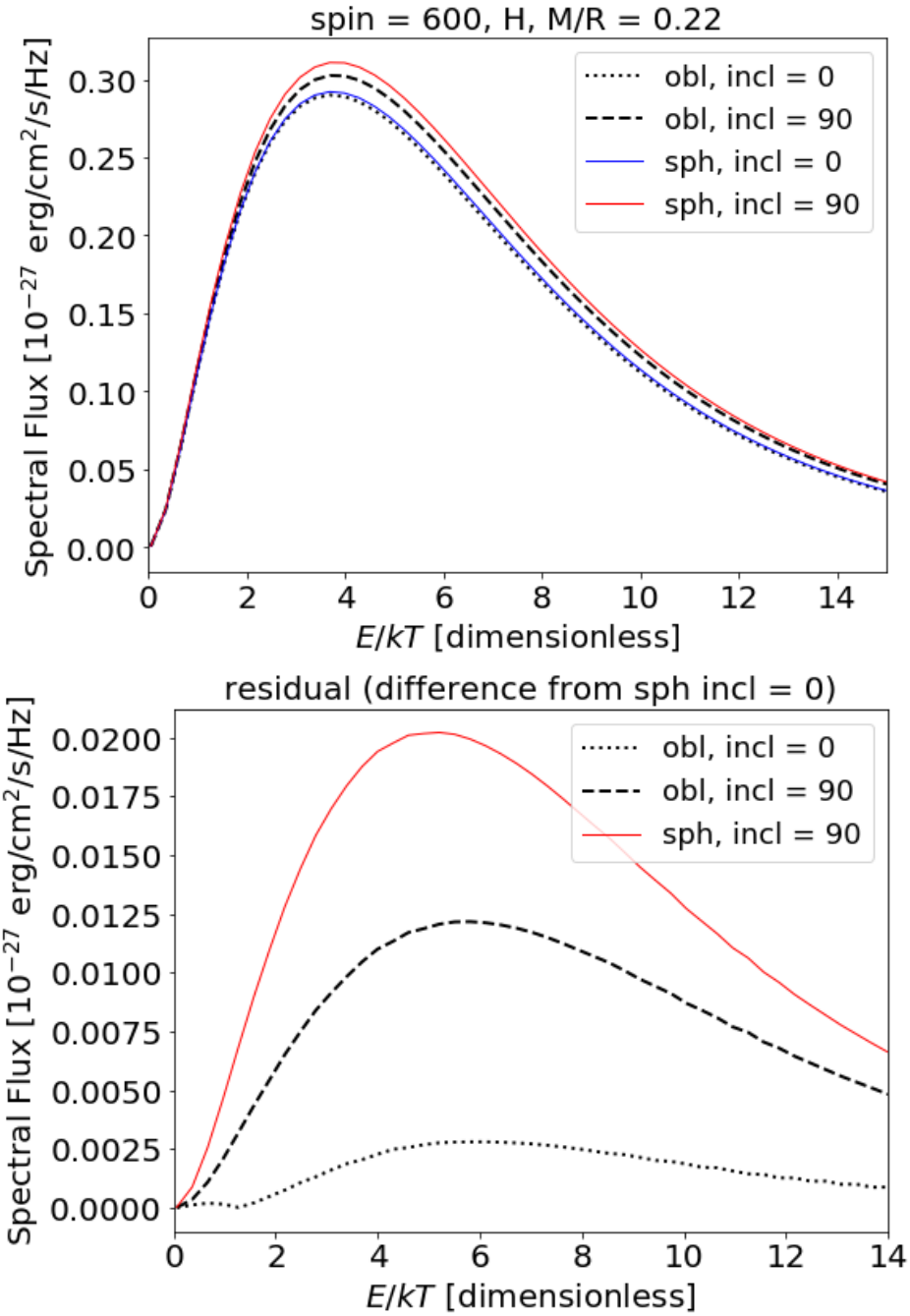

Figure 4.15: Top: Spectral flux at varying inclinations for both spherical and oblate NSs using a hydrogen atmosphere model with spin fixed at 600 Hz ($n\theta = 30$). For high inclinations, spherical stars have larger fluxes than oblate stars; they are nearly identical at low inclinations. Bottom: Difference as measured from the spherical $i = 0°$ curve.

Chapter 5

Conclusions and Future Work

We have designed a code which simulates bolometric and spectral flux for (in the most complex case) a rapidly rotating, oblate, relativistic NS with a hydrogen atmosphere. Preliminary tests of static, spherical NSs with blackbody emission agree with theoretical expectations. Although Doppler boosting (see Figure 2.7) and gravitational redshift (see Figure 4.5—also includes light bending) are by far the dominant effects, oblateness has a significant impact on flux (see Figures 4.8 and 4.9). H atmosphere models are vital as well; although the bolometric fluxes of blackbody and H atmosphere models are very nearly the same, the spectra are completely different (see Figure 4.4).

Considering these effects together is important because interactions exist between them—scattering in the H atmosphere should reduce oblateness and Doppler boosting effects through increased limb darkening, for example. If the variation in inclination continues to be larger with an H atmosphere even with improved grid resolution, then more investigation will be necessary to explain this behavior. Other interactions may also exist, which could become apparent at higher resolutions in future work.

Our code simulates a NS spectra given (among other inputs) a particular radius. Learning about NSs from real data involves working in the other direction—taking a spectral flux and using it to estimate the compactness ra-

tio (M/R). Potential EOS can be excluded based on this ratio, with the ultimate goal being to find the single EOS which describes NS matter. Although surface emission from NSs in qLMXBs has been observed using the Chandra and XMM-Newton X-ray telescopes, the limited resolution of these telescopes makes it difficult to calculate NS radii with the precision required to rule out all incorrect EOS. Many such accurate measurements of NS parameters will be required to deduce the correct NS EOS.

In the future, we will examine how flux changes with different values of compactness (M/R). It would also be interesting to use different atmosphere models (perhaps a helium atmosphere), since the composition of the atmosphere changes the spectral flux significantly. We will continue to work on optimizing the interpolation algorithm to ensure reasonable run times. We may also alter the grid on which the integration over the NS surface is performed, to avoid the increasing error near the poles.

The proposed X-ray telescope ATHENA will have considerably higher resolution, making future measurements more lucrative. ATHENA's increased sensitivity in the lower range will be particularly advantageous, since NS temperatures tend to be close to our chosen value of 10^6 K/0.26 keV (though they can vary by $\pm 10\%$). ATHENA's larger effective area will also allow for the detection of fainter NSs, as well as reducing error in flux measurements. Including all effects—including second order (transverse) Doppler effects and oblateness—will become increasingly important in the new era of higher resolution X-ray astronomy.

Bibliography

Abbott, B. P., Abbott, R., Abbott, T. D., et al. 2018, Physical Review Letters, 121, 161101

Akiyama, K., Alberdi, A., Alef, W., & Asada, K. 2019, arXiv:1906.11243 [astro-ph], doi:10.3847/2041-8213/ab1141, arXiv: 1906.11243

AlGendy, M., & Morsink, S. M. 2014, The Astrophysical Journal, 791, 78

Alpar, M. A., Cheng, A. F., Ruderman, M. A., & Shaham, J. 1982, Nature, 300, 728

Anand, J. D., Bhattacharjee, P., & Biswas, S. N. 1980, Journal of Physics A Mathematical General, 13, 3105

Andrew Lyne, & Graham-Smith, F. 1998, Pulsar Astronomy, 2nd edn. (Cambridge University Press)

Baade, W., & Zwicky, F. 1934, Proceedings of the National Academy of Science, 20, 259

Baubock, M., Ozel, F., Psaltis, D., & Morsink, S. M. 2015, The Astrophysical Journal, 799, 22, arXiv: 1407.3277

Baym, G., & Chin, S. A. 1976, Physics Letters B, 62, 241

Bildsten, L. 1998, NATO Advanced Science Institutes (ASI) Series C, 515, 419

Brown, E. F., & Bildsten, L. 1998, 19th Texas Symposium on Relativistic Astrophysics and Cosmology, 319

Cadeau, C., Morsink, S. M., Leahy, D., & Campbell, S. S. 2007, The Astrophysical Journal, 654, 458

Carroll, B., & Ostlie, D. 2007, An Introduction to Modern Astrophysics, 2nd edn. (Pearson Education)

Catuneanu, A., Heinke, C. O., Sivakoff, G. R., Ho, W. C. G., & Servillat, M. 2013, The Astrophysical Journal, 764, 145

Chen, H.-H., Ruderman, M. A., & Sutherland, P. G. 1974, The Astrophysical Journal, 191, 473

Clark, G. W. 1975, The Astrophysical Journal, 199

Degenaar, N., & Suleimanov, V. F. 2018, arXiv e-prints, arXiv:1806.02833

Duncan, R. C., & Thompson, C. 1992, The Astrophysical Journal, 392, L9

Fu, A., & Taam, R. E. 1990, The Astrophysical Journal, 353, 205

Gold, T. 1968, Nature, 218, 731

Gonzalez-Caniulef, D., Guillot, S., & Reisenegger, A. 2019, arXiv e-prints, arXiv:1904.12114

Harding, A. K., & Lai, D. 2006, Reports on Progress in Physics, 69, 2631

Heinke, C. O., Grindlay, J. E., Lugger, P. M., et al. 2003, The Astrophysical Journal, 598, 501

Heinke, C. O., Rybicki, G. B., Narayan, R., & Grindlay, J. E. 2006, The Astrophysical Journal, 644, 1090, arXiv: astro-ph/0506563

Hessels, J. W. T., Ransom, S. M., Stairs, I. H., et al. 2006, American Astronomical Society Meeting Abstracts #207, 207, 209.07

Hewish, A., Bell, S. J., Pilkington, J. D. H., Scott, P. F., & Collins, R. A. 1968, Nature, 217, 709

Ho, W. C. G., & Heinke, C. O. 2009, Nature, 462, 71

Ho, W. C. G., & Lai, D. 2001, Monthly Notices of the Royal Astronomical Society, 327, 1081, arXiv: astro-ph/0104199

Lorimer, D. R. 2008, Living Reviews in Relativity, 11, 8, arXiv: 0811.0762

Miller, M. C., & Lamb, F. K. 1998, The Astrophysical Journal, 499, L37

Morsink, S. M., Leahy, D. A., Cadeau, C., & Braga, J. 2007, The Astrophysical Journal, 663, 1244, arXiv: astro-ph/0703123

Nagase, F. 1989, Publications of the Astronomical Society of Japan, 41, 1

Ostriker, J. P., & Gunn, J. E. 1969, The Astrophysical Journal, 157, 1395

Papitto, A., Torres, D. F., Rea, N., & Tauris, T. M. 2014, Astronomy and Astrophysics, 566, A64

Pechenick, K. R., Ftaclas, C., & Cohen, J. M. 1983a, The Astrophysical Journal, 274, 846

—. 1983b, The Astrophysical Journal, 274, 846

Poutanen, J., & Gierlinski, M. 2003, Monthly Notices of the Royal Astronomical Society, 343, 1301, arXiv: astro-ph/0303084

Rajagopal, M., & Romani, R. W. 1996, The Astrophysical Journal, 461, 327

Read, J. S., Lackey, B. D., Owen, B. J., & Friedman, J. L. 2009, Physical Review D, 79, 124032

Rindler, W. 1991, Introduction to Special Relativity, 2nd edn. (Oxford University Press)

Rutledge, R. E., Bildsten, L., Brown, E. F., Pavlov, G. G., & Zavlin, V. E. 1999, The Astrophysical Journal, 514, 945, arXiv: astro-ph/9810288

—. 2002, The Astrophysical Journal, 578, 405

Rybicki, G. B., & Lightman, A. P. 1979, Radiative Processes in Astrophysics (John Wiley & Sons)

Shu, F. H. 2010, The Physics of Astrophysics Volume I: Radiation (Mill Valley, Calif.: University Science Books)

Watanabe, G., Iida, K., & Sato, K. 2000, Nuclear Physics A, 676, 455

Zavlin, V. E., Pavlov, G. G., Sanwal, D., et al. 2002, The Astrophysical Journal, 569, 894

Zavlin, V. E., Pavlov, G. G., & Shibanov, Y. A. 1996, Astronomy and Astrophysics, 315, 141